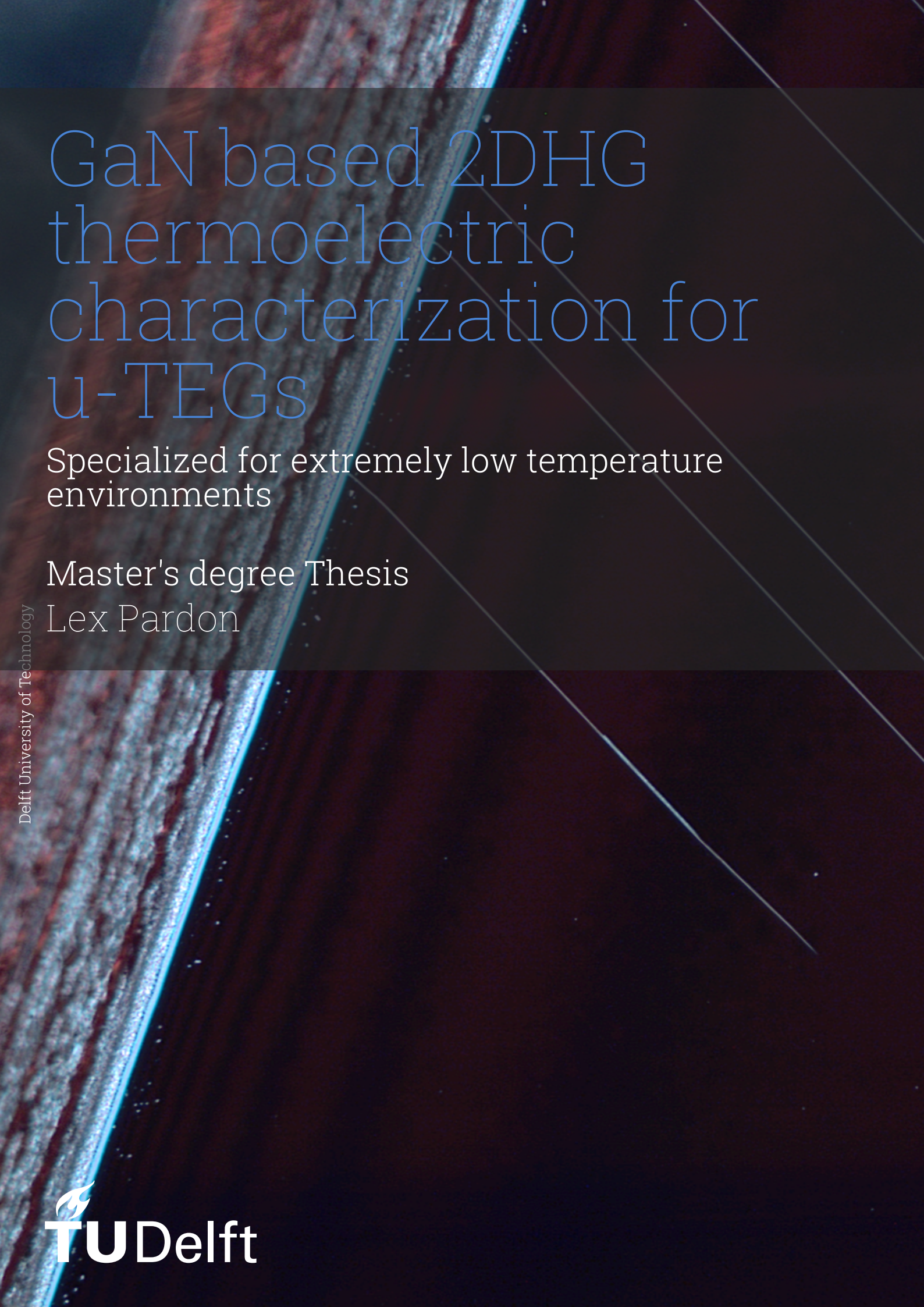


GaN based 2DHG thermoelectric characterization for u-TEGs

Specialized for extremely low temperature environments

Master's degree Thesis

Lex Pardon

Delft University of Technology

TU Delft

GaN based 2DHG thermoelectric characterization for u-TEGs

Specialized for extremely low temperature environments

by

Lex Pardon

In partial fulfillment of the requirements for the degree of

Master of Science
in Electrical Engineering

at the Delft University of Technology

Date:	Wednesday 2nd October, 2024
Supervisors:	K. Dowling
	F. Arroyo Cardoso
Defense Committee:	F. Sebastiano
	K. Dowling
	F. Arroyo Cardoso

An electronic version of this thesis is available at http://repository.tudelft.nl/
Cover image: Microscope image of Gallium Nitride wafer edge, showing stress-induced cracks

TU Delft

Acknowledgements

I want to express my deepest gratitude to those who supported me during the completion of this work.

First and foremost, I would like to thank **Karen Dowling**, who provided the opportunity to work on a project that was engaging, challenging, and, most importantly, educational to me. I would also like to thank both **Karen** and **Filipe Arroyo Cardoso** for their guidance throughout the project, including the constructive and eye-opening feedback and knowledge provided throughout the year.

I would also like to thank **Fabio Sebastiano** for completing the thesis committee as chair and asking insightful and critical questions during the defense.

Thirdly, I would like to thank the technical support staff from the Electronic Instrumentation Lab, namely **Lukasz, Ron, Jeroen** and **Zu Yao**, for providing technical support regarding the bonding of samples, the use of measurement equipment, and setting up measurement setups. I would also want to give an honorable mention to the technicians at QuTech (**Erik** and **Jason**), who have provided valuable information about vacuum equipment and general cryogenic equipment handling.

A special thanks to my colleagues and fellow students from the MUSIC lab, **Jannik, Jacopo, Floris, Yuxuan** and **Stefhen**, for both sharing their exciting projects and being great discussion partners when needed. I would also like to thank all other colleagues from the Electronic Instrumentation Lab, **Xiaoxi, Nuriel, Nandor, Sundeep, Alireza, Karim, Imad, Qiuxuan, Xinyi, Piet, Lucia** and many others, for creating a great environment to work in.

I would like to properly thank both my parents, **Hans** and **Anja**, and of course, my brother **Max**. Thank you for supporting me from the start of my career until now, getting me into electronics initially, and always encouraging me to continue. Of course, I would also like to thank **Tabea** for being supportive and providing a distraction from this work when things didn't go as smoothly.

A last thank you to the friends I made along the way through Plankenkoorts and the master's program, who provided an outlet for distraction but also helped with motivation to pull through during exam periods.

Lex Pardon
Delft, October 2024

Abstract

Thermoelectric generators (TEGs) are critical in environments where alternative energy harvesting methods are necessary, such as space exploration. This thesis investigates using a two-dimensional hole gas (2DHG) as a p-type material within a Gallium Nitride (GaN) based TEG. This study focuses on determining the thermoelectric performance of the 2DHG by measuring the Seebeck coefficient, electrical conductivity, and power factor for extremely cold environments.

This work introduces a novel simulation method used to evaluate different structures to find the optimal hole densities for maximizing the power factor (PF) of the 2DHG. A structure was realized, and its thermoelectric properties were experimentally assessed. Key results, including a Seebeck coefficient of $100 - 200\ \mu V/\Delta K$, a sheet resistance of $70 - 120\ k\Omega_{\square}$, and a resulting Power Factor (PF) of $60 - 100\ \mu W m^{-1} K^{-2}$, are measured over an extremely low-temperature range of 50 - 300 Kelvin and discussed for future applications.

These results demonstrate that GaN-based TEGs can significantly broaden the temperature range and improve the performance of TEGs in extreme conditions. These findings pave the way for more efficient thermoelectric systems, with potential applications in aerospace, deep-space missions, and other challenging environments.

Contents

Preface i

Abstract ii

Nomenclature v

1 Introduction 1
1.1 Overview of TEGs in extreme-cold environments . . . 1
1.2 Thesis overview . . . 2

2 Background and state of the art 3
2.1 Working principle and performance metrics of thermoelectric generators . . . 3
2.2 Thermoelectric properties . . . 4
2.2.1 Seebeck effect . . . 4
2.2.2 Electrical conductivity . . . 5
2.2.3 Thermal conductivity . . . 5
2.3 Optimization and limitations of Doped semiconductors . . . 7
2.3.1 Optimization of Power Factor by carrier concentration . . . 7
2.3.2 Limitation of doped semiconductors . . . 7
2.4 Gallium Nitride as an alternative semiconductor . . . 9
2.4.1 GaN as harsh environment semiconductor . . . 9
2.4.2 Formation of 2DEG and 2DHG through induced polarization in GaN/AlGaN/GaN structures . . . 9
2.4.3 Controllability of well-depth and sheet density with practical growth limitations . . . 11
2.5 State of the Art . . . 11
2.5.1 AlGaN/GaN 2DEG TEGs . . . 11
2.5.2 State of the art GaN 2DHG structures . . . 12
2.6 Conclusion . . . 13

3 Theoretical simulations and results 14
3.1 Sheet hole density and band energy level simulations using Schrödinger-Poisson solver 15
3.2 Electrical mobility and conductivity model . . . 17
3.2.1 Average scattering time and mobility . . . 17
3.2.2 Energy dependent scattering in 2-Dimensional inversion layer . . . 17
3.2.3 Scattering mechanisms . . . 17
3.2.4 Model validation using state-of-the-art . . . 19
3.3 Seebeck coefficient model . . . 20
3.3.1 Model validation using state-of-the-art . . . 21
3.4 Thermal conductance . . . 23
3.4.1 Overall thermal conductance of stack-up . . . 23
3.4.2 Thermal conductance of single layers . . . 23
3.4.3 Phonon scattering . . . 23
3.4.4 Results . . . 24
3.5 Structure optimization for 2DHG TEGs Power Factor . . . 25
3.5.1 Mg doped GaN surface charge depletion . . . 25
3.5.2 Hole density as a function of AlGaN layer properties . . . 26
3.5.3 Seebeck coefficient, Conductivity and Power Factor as a function of hole density 27
3.6 Proposed structures and expected performance . . . 30
3.7 Conclusion . . . 31

4 GaN 2DHG realization and fabrication 32
4.1 Devices under test, die size determination and measurement PCB design . . . 32

4.2 GaN on Silicon . . . 34
4.3 Ohmic contacts . . . 36
4.3.1 Ni/Au contact to p-GaN . . . 36
4.3.2 Tunneling behaviour through p-GaN/u-GaN to 2DHG . . . 36
4.3.3 Titanium Gold bonding contacts . . . 36
4.4 Metal contact fabrication and results . . . 37

5 2DHG measurement results and discussion 40
5.1 Measurement setups . . . 40
5.2 Measurement results . . . 42
5.2.1 I-V characteristics metal contacts . . . 42
5.2.2 Four-point sheet resistance measurements . . . 43
5.2.3 Seebeck coefficient measurements . . . 44
5.2.4 Power Factor . . . 46
5.3 Discussion . . . 47
5.3.1 Power Factor of 2-Dimensional electron and hole gas based TEGs . . . 47
5.3.2 GaN TEGs for extreme environments . . . 47

6 Conclusion 48
6.1 Main findings of this thesis . . . 48
6.2 Outlook on future works . . . 48

References 50

A Measurement error determination 53

B Complete flow-chart of fabrication process 55

C Dicing map 63

D Cryo-cooler user guide 65
D.1 Equipment . . . 65
D.2 Using Procedure . . . 65
D.2.1 Opening the vacuum chamber, mounting and closing the vacuum . . . 65
D.2.2 Closing the chamber and pumping down to vacuum . . . 66
D.2.3 Cooling down, controlling the cryo-cooler . . . 66
D.2.4 Warming up and opening again . . . 66
D.2.5 Long-time storage . . . 67
D.3 Other notes . . . 67

Nomenclature

Abbreviations

TEG Thermoelectric Generator

RPS radioisotope power system

AlGaN Alluminium Gallium Nitride

GaN gallium nitride

2DEG 2-Dimensional Electron Gas

2DHG 2-Dimensional Hole Gas

FEM Finite Element Method

BTE Boltzmann Transport Equation

XRD X-Ray Diffraction

QW Quantum-Well

PF Power Factor

HEMT High Electron Mobility Transistor

FoM Figure of Merit

MOCVD MetalOrganic Chemical Vapour Deposition

PCB printed circuit board

Si Silicon

Au Gold

Ni Nickel

Ti Titanium

Mg Magnesium

DUT Device Under Test

SMU Source Measure Unit

DMSO Dimethylsulfoxide

NH4OH Ammonium hydroxide

Symbols

Symbol	Definition	Unit
I	Electrical current	[A]
V	Voltage	[V]
n_s	hole or electron sheet density	[cm^{-2}]
n_i	intrinsic ionized charge carriers	[cm^{-3}]
n_e	extrinsic ionized charge carriers	[cm^{-3}]
E	Energy	[eV]
N_A	Dopant concentration	[cm^{-3}]
t	Thickness	[m]
m_e	Electron mass	[kg]
m_h	Hole mass	[kg]
x	Aluminum content inside $Al_xGa_{(1-x)}N$	[%]
k	Thermal conductivity	[$\frac{W}{m \cdot K}$]
T	Temperature	[K]
T_{avg}	Average temperature	[K]
ΔT	Temperature difference	[ΔK]
S	Seebeck coefficient	[$\frac{V}{\Delta T}$]
ρ	Resistivity	[$\Omega \cdot m$]
σ	Conductivity	[$S \cdot m^{-1}$]
PF	Power Factor	[$\frac{W}{m \cdot \Delta K^2}$]
R_{sh}	Sheet Resistance	[$\Omega_{\square}$]

1 Introduction

1.1. Overview of TEGs in extreme-cold environments

Thermoelectric Generators (TEGs) are widely adapted in conventional machines and devices that require either electric power generation. These devices, also known as peltier devices, are commonly used to harvest energy from a temperature gradient [18].

TEGs are mostly popular for their small form factor, ease of use, and durability. TEGs are often used to generate electric power from the rest-heat of industrial processes or can be used with alternative heat sources such as radio-isotopic decay, commonly known as radioisotope power system (RPS). RPSs are commonly used in satellites or off-earth exploration vehicles, where conventional fuel-based or solar-based energy sources are inefficient or impossible due to the remoteness of the application.

The use of RPSs in deep-space exploration is limited by its decline in efficiency with lower ambient temperatures as these devices move further away from the sun. Within an RPS, the TEG is the most critical device with a diminishing efficiency if temperatures drop below its semiconductors' freeze-out temperature. The most common semiconductor materials used in commercially available TEG are listed in Table 1.1, which are split into three different categories, low-temperature, Therefore, further investigation of alternative semiconductor materials is required to enable extremely low-temperature functionality of TEGs.

Material	**Temperature range, K**
Bi_2Te_3 alloy	Low temperature 300 - 400
PbTe alloy	Medium temperature 315 - 600
TiO_2	Medium temperature 425 - 650
SiGe	High temperature 620-730

Table 1.1: Different commercially available TEG materials, as reviewed by Zulkepli et al.[41]

Concluding from this overview of differently available materials, it can be stated that most commercially available materials are optimal for a fixed operating range.

A semiconductor material that is well known for its resilience to extremely harsh environments is gallium nitride (GaN). GaN is a wide-bandgap semiconductor, which gives it its harsh environment functionality. This material does not only perform well in high-temperature scenarios due to its high band-gap but is also well known for its low sheet resistance when carefully layered with a Alluminium Gallium Nitride (AlGaN) alloy to create a heterostructure [2, 25]. This heterostructure forms a layer of highly conductive electrons or holes, which helps increase the efficiency of electrical devices such as transistor, magnetic sensors and TEGs.

These induced thin layers of holes or electrons are known as a 2-Dimensional Electron Gas (2DEG) or 2-Dimensional Hole Gas (2DHG). These induced layers are not only known for their outstanding performance in the electrical domain but are also known to be extremely stable at extremely low temperatures[25]. Therefore, they are a potential candidate for improved TEGs in extremely cold environments.

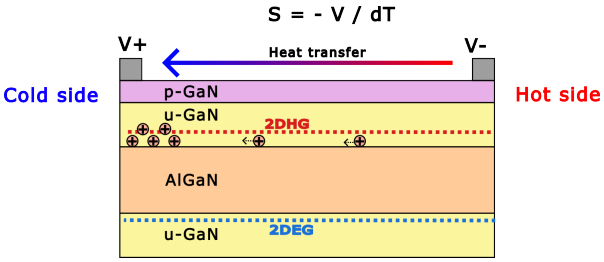


Figure 1.1: The Seebeck effect over a Galium-Nitride based 2-dimensional hole gas, where a voltage is induced by the Seebeck effect

Characterization of GaN TEGs has already been initiated in 2019 by Yalamarthy et al [28, 35, 29, 36], by investigating the thermoelectric properties of a GaN hetero-structure that induce a layer of highly conductive electrons at low temperatures. This research has proven the potential benefits of GaN TEGs in cold environments over different materials. This earlier work, however, solely characterized induced 2DEGs and recommends further research in a hole-based positive type counterpart known as a 2DHG to further improve GaN TEGs, as illustrated in Figure 1.1.

1.2. Thesis overview

This thesis' goal is to characterize the thermoelectric properties of a GaN heterostructure induced 2DHG. This thesis reports the steps taken and decisions made during this process and has been structured in the following chapters.

This thesis first introduces the background information required in 2 to further understand TEG performance metrics, such as the thermoelectric properties of semiconductors and expands upon the use of alternate materials and the use of GaN/AlGaN Quantum-Wells (QWs), as well as state-of-the-art in chapter 2. The thesis next moves to describe simulations of the earlier introduced mechanisms and verifies its results with the help of State-of-the-art literature in chapter 3. As a result, different structures are proposed to realize a 2DHG. 4 then discusses the challenges to realize the simulated structures, including methods to properly contact the 2DHG and how to reliably characterize its properties. The now fabricated structures are then characterized in chapter 5, where the measurement setup is introduced and measurement results are discussed. A final conclusion and discussion is formed in 6.

2

Background and state of the art

This chapter introduces the background information required to understand further GaN based TEGs. First, the basic working principles and physical properties of TEGs are reviewed. Then, the properties and physics of GaN semiconductors is explained by introducing the formation of a 2DEG and 2DHG inside GaN/AlGaN/GaN double hetero-structures. Lastly, a review of state-of-the-art TEGs and GaN is presented.

2.1. Working principle and performance metrics of thermoelectric generators

A simplified model of a TEG is provided in Figure 2.1. It is comprised of both an n-type and p-type semiconductor thermally connected in parallel and electrically connected in series. As seen in the figure, a temperature difference is applied between the hot and cold side. The temperature gradient over the semiconductor induces an electric field through diffusion. As a result, a harvestable voltage difference between the hot and cold side of the semiconductor can be used for power generation.

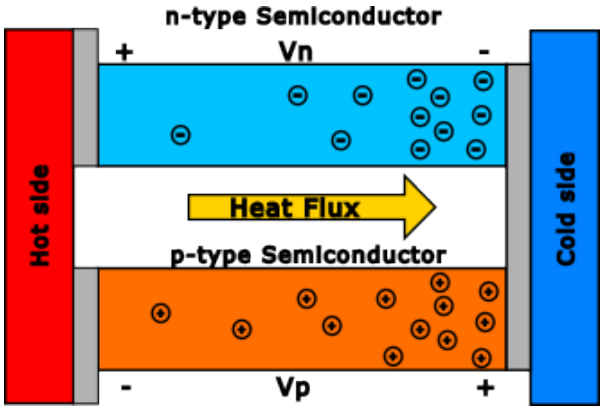


Figure 2.1: Simplified model of TEG, with grey representing electrically conducting materials

To efficiently harvest energy from a TEG, the connected load resistance must equal the TEGs internal resistance. Since the output power of the generator is related to both the generated voltage and the resistance of the TEG, the output power of the device can be expressed as $P = V^2/R_{TEG}$, where V is the generated voltage by the Seebeck-effect and R the internal resistance of the whole TEG. The thermoelectric properties of different semiconductor materials are commonly compared by comparing their power density, commonly known as the Power Factor (PF). The PF can be estimated using Equation 2.1, where S is the Seebeck coefficient and σ is the conductivity.

$$PF = \frac{S^2}{\rho} = S^2\sigma \tag{2.1}$$

To further compare different semiconductor materials, it is important to include the loss of energy through thermal conductivity (k). Where a high amount of heat transport between the hot and cold side is seen as an inefficiency. A common method to compare the efficiency of TEG materials is the Figure of Merit (ZT) where the PF is divided by the thermal conductivity as seen in Equation 2.2.

$$zT = \frac{S^2\sigma}{k}T \tag{2.2}$$

Both the PF and Figure of Merit (FoM) are used to compare different TEG-materials, most commonly plotted over temperature to determine their optimum temperature range.

2.2. Thermoelectric properties

The zT and PF metrics are commonly used to compare different semiconductor materials over different temperature ranges, providing the opportunity to choose the most efficient material for applications in specific operational temperatures. The thermoelectric properties directly affecting zT and PF can be optimized by chosing the optimal charge-carrier density. To get a better understanding of how both ambient temperature and electron and hole density affect the Seebeck effect, conductivity, and thermal conductivity, these thermoelectric properties are further introduced in this section.

2.2.1. Seebeck effect

The Seebeck effect is a coupling mechanism between charged particle transport and heat transport. The displacement of charges due to this coupling mechanism generates an electric field that is linearly dependent on the temperature gradient applied to the semiconductor. This linear relation is expressed in Equation 2.3, where V represents the generated voltage of the electric field and ΔT represents the temperature difference over the semiconductor.

$$V_{TEG} = S \cdot \Delta T \tag{2.3}$$

To derive the Seebeck coefficient for a specific material, a more in-depth analysis of the transport mechanisms inside semiconductors is required [12, 28]. By expressing the current flux (J_e, Equation 2.4) and the heat flux (J_q, Equation 2.5) of a semiconductor with a temperature and voltage gradient using Onsager relations [12], the direct relation between voltage and temperature can be expressed. Here L_{11} represents the electrical conductivity of the semiconductor, L_{12} represents the coupling coefficient between the current and temperature gradient, L_{21} represents the energy carried due to convection of electrons under an electrochemical potential gradient and L_{22} represents the diffusion of electrons under a temperature gradient.

$$J_e = L_{11}\left(-\frac{dV}{dx}\right) + L_{12}\left(-\frac{dT}{dx}\right) \tag{2.4}$$

$$J_q = L_{21}\left(-\frac{dV}{dx}\right) + L_{22}\left(-\frac{dT}{dx}\right) \tag{2.5}$$

If the temperature gradient over the material is zero, a relation between J_q and J_e can be derived as seen in Equation 2.6, commonly known as the Peltier effect. Here, Π represents the Peltier coefficient, which corresponds to the heat flow through a material when a current is applied. This principle is commonly used to fabricate Peltier coolers and is directly related to the Seebeck coefficient as $\Pi = ST$, where T is the temperature. The Seebeck coefficient can be rewritten as seen in Equation 2.7, showing the direct relation between the coupling coefficient between current and temperature gradient (L_{12}) and the electrical conductivity (L_{11}).

$$J_q = \frac{L_{21}}{L_{11}}J_e = \Pi J_e \tag{2.6}$$

$$S = -\frac{dV}{dT} = -\frac{V}{\Delta T} = \frac{L_{12}}{L_{11}} \tag{2.7}$$

By now expressing L_{11} and L_{12} using the Boltzmann Transport Equation (BTE), an analytical expression for the Seebeck coefficient can be found as seen in Equation 2.8, 2.9, 2.10 [12] where the integrals are taken from the bottom of the conduction band to infinity for electrons and from the top of the valence

band to minus infinity for holes. v represents the velocity of the carriers, $\tau(E)$ the scattering rate of the carriers as a function of energy, $g(E)$ the density of states, $f_0(E)$ the Fermi-Dirac distribution and E_F the Fermi level.

$$L_{11} = -\frac{e^2}{3}\int v^2\tau(E)\frac{\delta f_0}{\delta E}g(E)dE \tag{2.8}$$

$$L_{12} = \frac{e}{3T}\int v^2\tau(E)(E-E_F)\frac{\delta f_0}{\delta E}g(E)dE \tag{2.9}$$

$$S = -\frac{1}{qT}\frac{\int v^2\tau(E)(E-E_F)\frac{\delta f_0}{\delta E}g(E)dE}{\int v^2\tau(E)\frac{\delta f_0}{\delta E}g(E)dE} \tag{2.10}$$

The Seebeck coefficient is commonly rewritten as $S = -\frac{\int(E-E_F)\sigma(E)dE}{qT\int\sigma(E)dE}$ for bulk doped materials, where $\sigma(E)$ is the differential conductivity. From both the simplified expression and Equation 2.10 the conclusion can be drawn that the Seebeck coefficient is heavily dependent on the location of the Fermi-level in respect to the top of the conduction band or bottom of the valence band, represented by E_F in the equation.

2.2.2. Electrical conductivity

The electrical conductivity σ describes how well a semiconductor material conducts electrical current. High electrical conductivity is desired in TEGs to improving the output power of the device. σ is directly dependent on the mobility of the charge carriers (μ) and charge carrier density (n) as seen in Equation 2.11 ,where q represents the charge of the carrier. The charge carrier density is normally controlled by adding doping atoms to the semiconductor, increasing the conductivity of the material.

$$\sigma = q\mu n \tag{2.11}$$

The carrier mobility of semiconductors can be estimated by using Equation 2.12, where τ represents the total scattering time of a charge carrier in the lattice and m^* the effective mass of a charge carrier. The effective mass of a charge carrier is material-dependent, whereas the total scattering time is affected by both the semiconductor material and crystalline quality. In section 3.2, a more in-depth approximation of the material's conductivity in terms of scattering is investigated.

$$\mu = \frac{e\tau}{m^*} \tag{2.12}$$

2.2.3. Thermal conductivity

The thermal conductance noted as k, of a material, is expressed in [$W\cdot m^{-1}\cdot K^{-1}$] and is considered to be a loss of energy in TEGs as it enables the transfer of heat. Thermal conductivity in semiconductors is comprised of two distinct methods of heat transport, charge and phonon heat-carriers. The total thermal conductivity can thus be expressed using $k = k_p + k_e$, where k_p represents the thermal conductivity contribution by phonons and k_e the thermal conductivity contribution of electrons.

k_e can be estimated using Equation 2.13, where the relation between the thermal conductivity and electrical conductivity of electrons is directly related through the Wiedermann-Franz law [12] where L represents the constant Lorenz number, C_E the heat capacity of the heat carriers and v_F the average velocity of said carriers. From this relation, one can conclude that by increasing the charge carriers of a material, both the thermal and electrical conductivity increase.

$$k_e = \frac{1}{3}C_e v_F^2\tau_E = LT\sigma \tag{2.13}$$

The thermal conductance through lattice vibrations, commonly known as phonons, can be expressed using Equation 2.14, based on the BTE model, where the specific heat capacity $C(\omega)$, the specific velocity $v(\omega)$ and the mean free path $\lambda(\omega)$ of different phonon modes are integrated. To include the two transverse phonon modes and one longitudinal phonon mode for more general cases, a summation is taken. The mean free path $\lambda(\omega)$ can be estimated in the form of phonon scattering $\tau(w)$ multiplied by the phonon velocity $v(\omega)$.

$$k_p = \sum_{LA,TA} \frac{1}{3} \int C(\omega) v(\omega) \lambda(\omega) d\omega = \sum_{LA,TA} \frac{1}{3} \int C(\omega) (v(\omega))^2 \tau(\omega) d\omega \tag{2.14}$$

Due to the direct relation between the thermal and electrical conductivity of electrons, the thermal conductance can be minimized by decreasing the electrical conductivity. Therefore, the thermal conductance of lowly doped semiconductors is only comprised of the thermal conductance through lattice vibrations ($k = k_p$).

2.3. Optimization and limitations of Doped semiconductors

To optimize the zT and PF of TEGs, the semiconductor's charge carriers are heavily controlled by doping to influence their characteristics. This process is further explained below, including the negative consequences that this method of optimization introduces to TEGs.

2.3.1. Optimization of Power Factor by carrier concentration

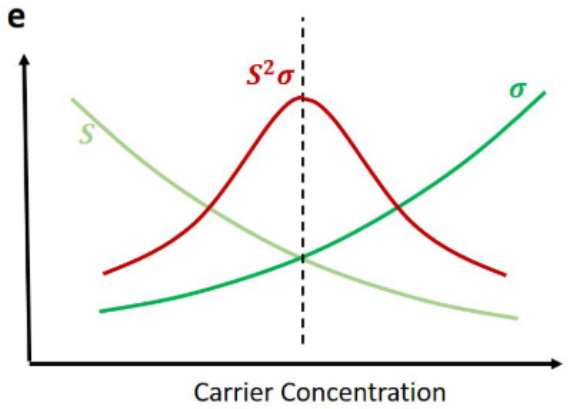


Figure 2.2: Seebeck, conductivity and Power Factor over carrier concentration [36]

Since the Seebeck-coefficient, electrical, and thermal conductivity is dependent on the carrier concentration, an optimum carrier concentration can be found to maximize both the PF and FoM. As the carrier concentration increases of a semiconductor, both the thermal and electrical conductivity increase but at the cost of a decrease in the Seebeck-coefficient.

The PF as expressed in Equation 2.1, is dependent on the Seebeck coefficient and electrical conductivity and represents the output power of a TEG leg. By plotting both the Seebeck-coefficient and electrical conductivity over different carrier concentrations in Figure 2.2 as well as the PF, it can be clearly stated that an optimum carrier concentration must be chosen. A similar optimization strategy is performed in this work, using an improved simulation method that is verified using state-of-the-art measurements.

2.3.2. Limitation of doped semiconductors

An important aspect of semiconductors is controlling the charge-carrier concentration through doping. Doping introduces extrinsic impurities into an otherwise pure semiconductor, allowing for precise control of its electrical properties. In a doped semiconductor, the total charge-carrier concentration (n_{tot}) is the sum of intrinsic carriers (n_i) and extrinsic carriers (n_e), which can be expressed as $n_{tot} = n_e + n_i$. Both intrinsic and extrinsic carriers are thermally excited, with their populations depending heavily on temperature. Semiconductors behave differently over temperature as the ionization of charge carriers is heavily dependent on it. The behavior of charge carriers can be categorized in three different regions over temperature: freeze-out, extrinsic, and intrinsic.

At low temperatures, the semiconductor operates in the freeze-out region. In this regime, the thermal energy available is insufficient to ionize the dopant atoms effectively, meaning that only a small portion of dopants contribute to free charge carriers. For instance, in an n-type semiconductor, the donor atoms remain largely neutral, with their electrons still bound to them. The carrier concentration at this point is minimal, as the thermal energy available is insufficient to excite the dopants. The hole density in a p-type semiconductor at low temperatures can be approximated using Equation 2.15, where N_A is the concentration of acceptor dopants, E_A is the dopant ionization energy, g is the degeneracy factor, and T is the temperature.

$$p = \frac{N_A}{1 + g \cdot exp(\frac{E_A}{k_B T})} \tag{2.15}$$

The freeze-out region is defined as the region where only a small portion of the dopants are excited and can be stated as $n_e << N_D$ or $p << N_A$.

As the temperature increases, the semiconductor enters the extrinsic region, where the majority of the dopants are ionized. Here, the thermal energy is sufficient to excite most of the dopants, allowing them to donate or accept electrons. The extrinsic carrier concentration stabilizes, and the majority of charge carriers are contributed by dopant atoms. In this temperature range, the extrinsic carrier concentration dominates over the intrinsic carrier concentration, such that $n_e >> n_i$. This region is considered the operational region of doped semiconductors as it can be reliably controlled by changing doping concentrations.

Lastly, at high temperatures, the semiconductor transitions into the intrinsic region, where the intrinsic carrier concentration (n_i) begins to dominate over the extrinsic carriers. In this regime, thermal energy is so high that a large number of electron-hole pairs are generated, overwhelming the contribution of the dopants. The intrinsic carrier concentration is governed by Equation 2.16, where T represents the temperature, E_g the band-gap energy of the semiconductor, and m_e and m_h the electron and hole mass, respectively. As T increases, the intrinsic carrier concentration increases drastically, where inevitably, a point is reached where the majority of carriers are dominated by intrinsic carriers, which can be stated as $n_i >> n_e$. This region is known as the intrinsic region and cannot be carefully controlled anymore through dopants.

$$n_i = 2(\frac{k_B T}{2\pi\overline{h}})^{3/2}(m_e m_h)^{3/4} exp[-\frac{E_g}{2k_B T}] \tag{2.16}$$

The desired region of operation, the extrinsic region, of a semiconductor material is therefore limited to a temperature range with no significant presence of intrinsic charge carriers and enough thermal energy to activate extrinsic charge carriers. This limiting operational temperature range impacts semiconductor materials performance as TEGs, where different materials outperform others for specific temperature ranges as seen in Figure 2.3, where the FoM falls drastically outside their optimal region. The need for a material that is able to function efficiently over a wide temperature range can, therefore, outweigh extremely high-efficiency devices in very narrow temperature ranges. This thesis, therefore, focuses on an alternative material with an extremely wide operating temperature range.

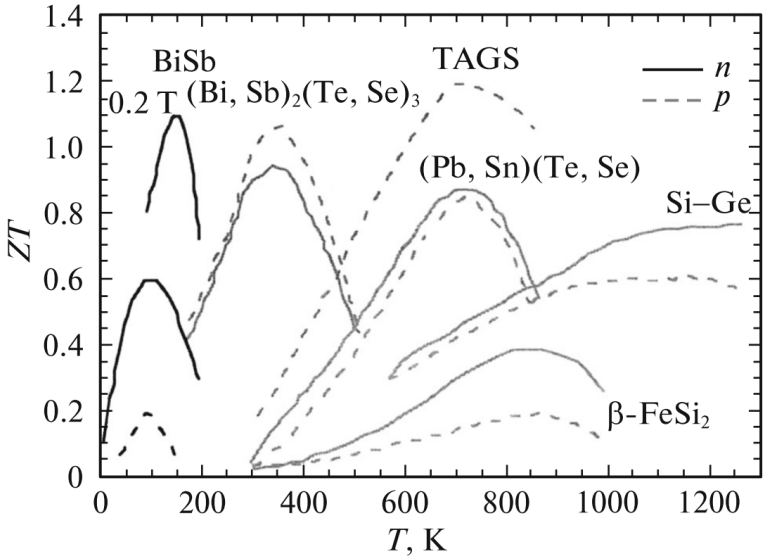


Figure 2.3: FoM (zT) of different thermoelectric materials over a temperature range of 0 - 1200 K [31]

As can be seen in Figure 2.3, the FoM of different materials is plotted over temperature. The majority of the materials shown in this graph have an optimal region of 200-400 Kelvin. Therefore, a material that is functional over an extremely wide temperature range can improve the useability of TEGs in use-cases where a wide operational temperature range is required.

2.4. Gallium Nitride as an alternative semiconductor

GaN is a promising semiconductor material, primarily known for its harsh environment functionality and high carrier mobility, and is already well adapted in the industry [14, 3]. This section introduces the background information required to further understand GaN and possible improvements to TEG efficiency.

2.4.1. GaN as harsh environment semiconductor

With its wide band-gap of 3.4 eV, when compared to other semiconductor materials like Silicon (1.12 eV), GaN is considered an extreme wide band-gap material. As mentioned in subsection 2.3.2, the band-gap of a semiconductor directly affects the minimum temperature of the intrinsic region of the semiconductor. An ultra-high band-gap semiconductor such as GaN increases the maximum operational temperature of semiconductors to up to 1000 degrees Celsius [14] compared to conventional materials.

The formation of a QW can be intrinsically induced at hetero-junctions made of AlGaN and GaN, forming a confined layer of electrons or holes. The formation of the so-called 2DEG and 2DHG are well known for their high mobility and independence of temperature at extremely low temperatures as they do not require extrinsic dopants to form [25].

The combination of the high bang-gap and formation of a temperature independent QWs results in GaN's ability to operate in an extremely wide temperature range, opening another path for extreme environment semiconductors. GaN is therefore considered a perfect candidate for further research and development as a TEG thermoelectric material.

2.4.2. Formation of 2DEG and 2DHG through induced polarization in GaN/AlGaN/GaN structures

The formation of a 2DEG and 2DHG is realized through the formation of a GaN/AlGaN/GaN double hetero-junction, in which the polarizing effect of the AlGaN induces a thin negatively charged layer in one GaN/AlGaN heterojunction and a positively charged layer in the other hetero-junction. To get a better understanding of how the induced 2DEG and 2DHG form, the induced polarization of the AlGaN layer must be further explained.

III-V nitrite semiconductors are commonly known for their wurtzite crystal structures that is grown through MetalOrganic Chemical Vapour Deposition (MOCVD). These wurtzite crystal structures are typically grown into the $[0001]$ or $[000\bar{1}]$ direction, commonly known as the c-plane. As can be seen in Figure 2.4, an a-symmetry is present in the [0001] direction, which results in piezo-electric properties of the deposited layer.

The crystal structure shown in Figure 2.4 represents the structure of a GaN wurtzite crystal. By partially replacing Gallium atoms with Aluminum atoms, a ternary alloy is created of $Al_xGa_{1-x}N$ in which x denotes the percentage of Aluminum to Gallium. The lattice constant of said $Al_xGa_{1-x}N$ will change as a function of x compared to normal GaN. In a GaN/AlGaN hetero-junction, the lattice mismatch introduces strain to the AlGaN layer. The induced strain on the AlGaN creates an electric field due to its piezoelectric properties and can be used to create a intrinsic polarization layer within the structure.

This polarization translates into a noticeable electric field over the AlGaN layer of up to 2 MV/cm which can be intrinsically induced by varying the AlGaN Aluminum content [1]. This electric field can be estimated using Equation 2.17, where ϵ represents the permittivity of AlGaN, P_{sp}^{AlGaN} represents the spontaneous polarization and $P_{pz}^{AlGaN}(x)$ represents the piezoelectric polarization as a function of the aluminum content x, further estimated by [1]. The charge density on the surfaces of the AlGaN as a result of the piezoelectric and spontaneous polarization can be expressed using Equation 2.18, where q represents the elementary charge. This charge difference is later seen in Figure 2.5, which attracts holes for the negatively charged side, and electrons on the positively charged side.

$$E_{AlGaN} = \frac{P_{pz}^{AlGaN}(x) + P_{sp}^{AlGaN}}{\epsilon_{AlGaN}} \tag{2.17}$$

$$\sigma_{AlGaN} = \pm(P_{pz}^{AlGaN}(x) + P_{sp}^{AlGaN}) \cdot -q \tag{2.18}$$

Figure 2.5 provides an overview of a pGaN-GaN-AlGaN-GaN structure commonly used to form both a 2DEG and 2DHG, where a surface charge profile and a band-diagram sketch is provided to provide

a more elaborate look into the formation of said QWs. Sub-figure A represents a not-to-scale complete structure and the location of the formed 2DEG and 2DHG.

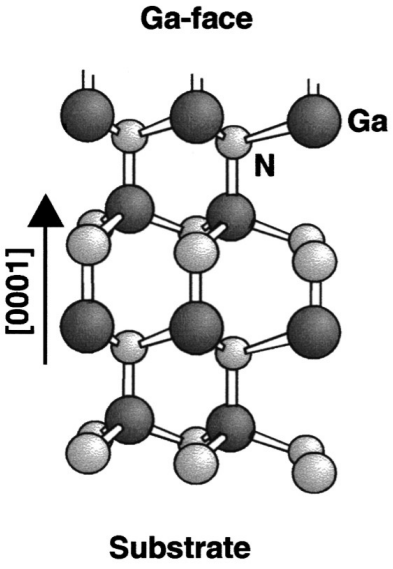


Figure 2.4: Wurtzite crystal structure of GaN, showing a-symetry on the [0001] axis[2]

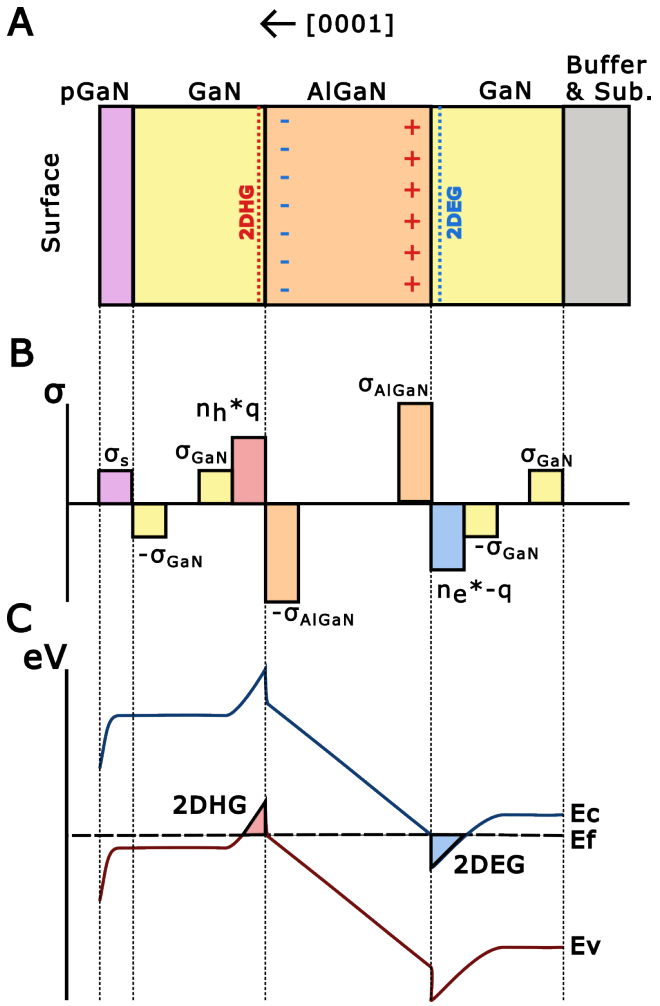


Figure 2.5: A: typical pGaN-GaN-AlGaN-GaN double heterostructure layout with marked 2DEG and 2DHG regions.
B: Surface charge model of typical double-heterojunction.
C: Band-diagram sketch of double-heterojunction with marked 2DEG and 2DHG regions

A common approach to find the sheet density of a 2DEG or 2DHG is the use of a surface-charge model, in which the intrinsic surface charge of the AlGaN layer at its hetero-junctions has already been determined in Equation 2.18. By stating that the net surface charge of a hetero-junction must be zero ($\sigma_{surface1}+\sigma_{surface2}=0$) and sketching a surface charge distribution of the entire structure in Figure 2.5 B, an expression for the 2DEG sheet density can be found as the surface charge can be related to its sheet density using 2.19.

$$n_e \cdot q = \sigma_{AlGaN} - \sigma_{GaN} \tag{2.19}$$

A similar approach is used to determine the sheet hole density of the formed 2DHG as seen in Figure 2.5 B, where the p-GaN helps with the surface charge depletion and the sign of the surface charge carriers is flipped as the AlGaN charge is now negative.

By sketching the band diagram, one can find out the well-depth of both QWs as the GaN becomes degenerate ($E_C < E_F$ or $E_V > E_F$). With the help of band-bending, the band-gap mismatch and polarizing effect of the AlGaN layer, the band-diagram can be seen in Figure 2.5 C. This band-diagram clearly shows the formation of a 2DEG and 2DHG on both sides of the AlGaN polarizing layer, as marked with the colored area of degeneracy.

One of the major benefits of an induced 2DEG or 2DHG is the high mobility of electrons and holes in the formed QW. No dopants are added to the area where the QW forms, significantly limiting the impurities added to the lattice structure. Lattice impurities in doped materials significantly decrease mobility, therefore having a lower conductivity. In formed QWs we can assume that impurity scattering caused by dopants is negligible, therefore increasing the conductivity of GaN QWs, directly improving the PF of TEGs. This benefit of GaN based devices is commonly seen in 2DEG-based High Electron Mobility Transistors (HEMTs) [10].

2.4.3. Controllability of well-depth and sheet density with practical growth limitations

As previously stated and confirmed by 2.19, the AlGaN layer properties, such as the thickness and aluminum content x, directly affect the electric field and charge profile of the structure. Where an increased aluminum content in the AlGaN results in a higher lattice mismatch, therefore increasing the piezoelectric charge denoted as $\pm\sigma_{pz}^{AlGaN}$. As 2.19 suggests, a higher polarizing AlGaN layer will induce a higher sheet density on both the Ga and N side of the AlGaN layer, increasing both the hole and electron sheet densities.

As changing the AlGaN properties opens possibilities to control the sheet density of the QWs, the lattice mismatch and, therefore, induced strain introduces a risk of cracking the grown wafers. The maximum limits of what aluminum content (x) and thickness the AlGaN layer can be grown is dependent the buffer layer and quality of the growing method.

As earlier mentioned in 2.3.1, an ideal carrier concentration for semiconductor materials can be found. During this thesis, an in-depth look will be taken to map the possible regions of what hole densities are possible and what the maximum Power Factor (PF) within this range is expected.

2.5. State of the Art

To further investigate the status of GaN based TEGs, an overview of state-of-the-art research is given below. From this, a research question for this thesis was formulated, and further steps can be carried out to improve knowledge and research on this topic.

2.5.1. AlGaN/GaN 2DEG TEGs

This work continues the pursuit of GaN based TEGs previously investigated by Yalamarthy et al. [35, 29]. Yalamarthy's work was dedicated to the development of an optimized 2DEG, investigating the n-type semiconductor leg possibilities of GaN. A GaN/AlGaN hetero-junction was observed for its thermo-electric properties over a wide range of different temperatures. By characterizing two different stack-ups, with differing GaN layer thicknesses, high [35], and low [29] operating temperature ranges were investigated.

A thin GaN layer thickness of 100 nm and a thick GaN layer thickness of 1.2 μm were compared, in which the transport of thermal energy is obstructed by the thinner GaN layer. A 4x improvement in the FoM (zT) has been observed in the thin GaN layer compared to externally doped GaN because of its improved conductivity. A PF of 4-7 $mWm^{-1}K^{-2}$ was observed for the formed 2DEG over a temperature range of 0 - 300 degrees C.

Further low-temperature measurements have lead to the discovery of a significant improvement of the PF in extremely cold environments for a thick GaN layer[29]. Phonon-drag is a phenomenon that couples the thermal conductivity to a generated voltage over a semiconductor and is considered to be an addition to the diffusive Seebeck-effect mentioned earlier in 2.2.1. Yalamarthy et al. have determined the presence of phonon-drag in extremely cold temperatures, further increasing the Seebeck coefficient in near-zero Kelvin environments. This additional improvement of the Seebeck-coefficient and PF further proves the usability of GaN based TEGs in further projects.

Yalamarthy's research was based on 2DEG based TEGs only. Therefore, this work will be primarily focused on 2DHG based TEGs optimization to further investigate the GaN based TEGs. Since the combination of an n-type and p-type semiconductor TEG is considered to be most optimal, this master thesis will further investigate structures that are able to form both a 2DEG and 2DHG, where the characterization of the formed 2DHG is considered to be the primary goal.

2.5.2. State of the art GaN 2DHG structures

By comparing different GaN based 2DHGs, a better overview of the possibilities can be provided. As seen in Table 2.1, different state-of-the-art 2DHG structures are compared.

	Structure type	2DHG density (cm^{-2})	2DHG mobility (cm^2/Vs)	2DEG
Chaudhuri et al. [8]	GaN/AlN heterojunction	$5 \cdot 10^{13}$	10	No
Beckmann et al. [4]	pGaN/GaN/AlGaN/AlN	$1.6 \cdot 10^{13}$	-	No
Nakajima et al. [23]	pGaN/GaN/AlGaN/GaN double heterojunction	$1 \cdot 10^{13}$	16	Yes
Shao et al. [30]	pGaN/GaN/AlGaN/GaN double heterojunction	$3.6 \cdot 10^{13}$	10	Yes

Table 2.1: Overview of different state-of-the-art 2DHG structures

From this overview, it can be stated that different structures can be used to reach a maximum hole sheet density of $5 \cdot 10^{13}$ and a maximum mobility of $16 cm^2/Vs$. Since the initial goal of this thesis is the investigation of a 2DHG as complementary p-type to an already characterized GaN based 2DEG, a double heterojunction that is can induce both a 2DHG and 2DEG is considered beneficial compared to a single heterojunction.

The use of a double heterojunction type structure is the most common method of inducing a 2DHG, therefore making it a more reliable method to form and characterize a 2DHG. A double hetero junction, as introduced and partially characterized by Nakajima et al. [23]. Nakajima et al. [25] has also proven the extremely low-temperature performance of said double heterojunction and further investigates the thickness of the unintentionally doped GaN thickness to improve mobility of the formed 2DHG. Therefore, it is the ideal structure to optimize and characterize as a TEG semiconductor material.

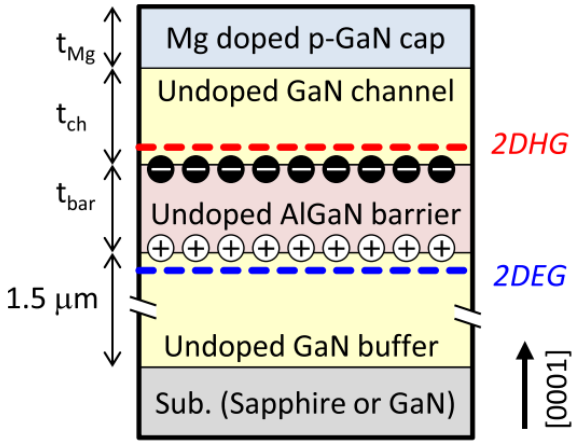


Figure 2.6: p-GaN/GaN/AlGaN/GaN structure proposed by Nakajima [24]

By comparing both the formed 2DHG and its mobility with a Magnesium (Mg) doped GaN bulk substrate, the temperature independence of a 2DHG formation has been proven by Nakajima up to temperatures down to 25 Kelvin [25]. Later, the mobility of the formed 2DHG has further been investigated, where the relation between the AlGaN layer thickness and sheet hole density is measured and proven. Further characterizations have been carried out to optimize the undoped GaN layer thickness to minimize impurity scattering due to dopants from the p-GaN diffusing into the undoped GaN layer where a 2DHG forms. Giving guidelines and limits of the proposed p-GaN/GaN/AlGaN/GaN structure[23].

Further research on the 2DHG mobility by Shao P. [30] confirms earlier works of Nakajima by investigating the mobility of 2DHGs formed through p-GaN/GaN/AlGaN heterojunctions. In which an increase

in mobility of the 2DHG was observed with colder temperatures, which in terms positively influences TEG performance in low temperatures.

2.6. Conclusion

In order to get closer to the use of GaN for an extremely wide temperature range TEGs, the next logical step to take is the optimization and realization of a GaN based 2DHG. By choosing a double-heterojunction structure, it is also possible to open future works to include a 2DEG to a single structure to enable the use of a TEG that is comprised of an n-type and p-type semiconductor. Therefore, this work will be mostly based on state-of-the-art GaN/AlGaN/GaN double heterojunction of which the 2DHG will be characterized for its thermo-electric properties to determine the feasibility to use GaN based TEGs.

The process to realize and characterize a GaN based 2DHG, is done by firstly simulating different structure properties, as done in chapter 3. After the carried out simulations, the GaN based TEG is then realized and characterized for final evaluations.

3

Theoretical simulations and results

To estimate the performance of the proposed double heterostructures, a method to approximate the characteristics of a 2DHG TEG is developed. Firstly, by dividing the estimation process into individual steps, a piece-wise approach is made to estimate the performance of the 2DHG. Figure 3.1 provides an overview of the different steps taken to assess the performance of the formed 2DHG, with structure properties such as layer composition and thickness as input. As seen in the figure, multiple intermediate steps are required to estimate the characteristics of a 2DHG. In this work, a novel method to improve the accuracy of the simulation results is introduced by directly using the Schrödinger-Poisson solvers results instead of re-calculating the energy levels in the matlab estimations.

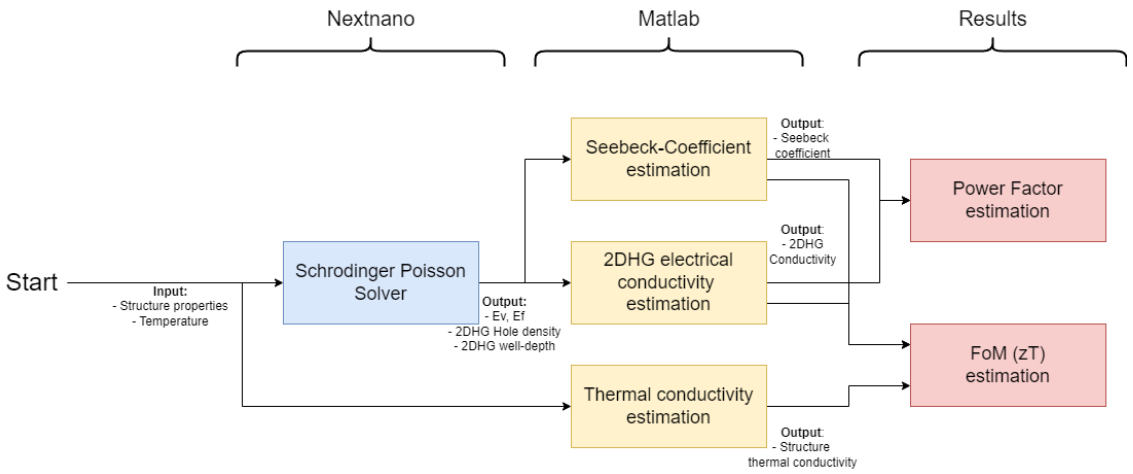


Figure 3.1: Overview of simulation steps

As seen in Figure 3.1, a piece-wise approach is taken where individual simulation steps are used to determine the overall characteristics of the structure. This chapter starts with describing the simulation models used and compares them with state-of-the-art measurements to determine the reliability of the following simulations:

- Schrödinger-Poisson solver, section 3.1
- Electrical mobility and conductivity model, section 3.2
- Seebeck coefficient model, section 3.3
- Thermal conductivity model, section 3.4

During the validation process, re-iterations of the simulation model have been carried out to optimize the simulation models for minimal estimation errors. After the validation and explanation of most models, the PF is optimized using the introduced models in section 3.5.

3.1. Sheet hole density and band energy level simulations using Schrödinger-Poisson solver

The simulation initially starts with a Schrödinger-Poisson solver, Nextnano [6]. A Schrödinger-Poisson solver is a computational tool used to self-consistently solve the Schrödinger equation, describing quantum mechanical wavefunctions, alongside the Poisson equation, which determines the electrostatic potential from charge distributions. This software package provides a self-contained Schrödinger-Poisson solver to estimate nanoscale semiconductor structures and devices. Nextnano can generate band diagrams of structures and calculate the hole and electron density at different locations within the structure, including properties such as strain, temperature, and material-dependent properties.

Figure 3.2 shows a band-diagram graph generated by Nextnano of a double heterostructure in which the polarization of the strained AlGaN can be observed. This figure shows the formation of a 2DEG and 2DHG.

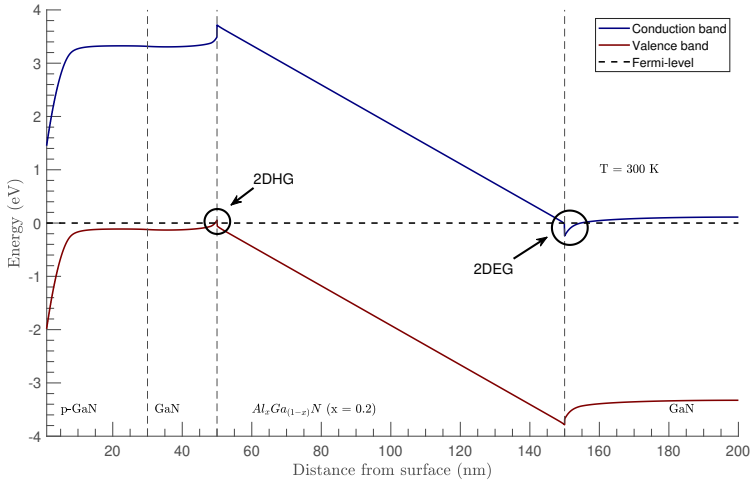


Figure 3.2: Band-diagram of pGaN-GaN-AlGaN-GaN structure

Figure 3.3 shows the hole and electron density within the same structure, in which a high concentration is observed where the semiconductors are considered degenerate. By taking the integral of the hole density over a 2DHG location, the sheet density of a 2DHG can be extracted for further use and evaluation. A similar approach can be taken to estimate the 2DEG sheet density.

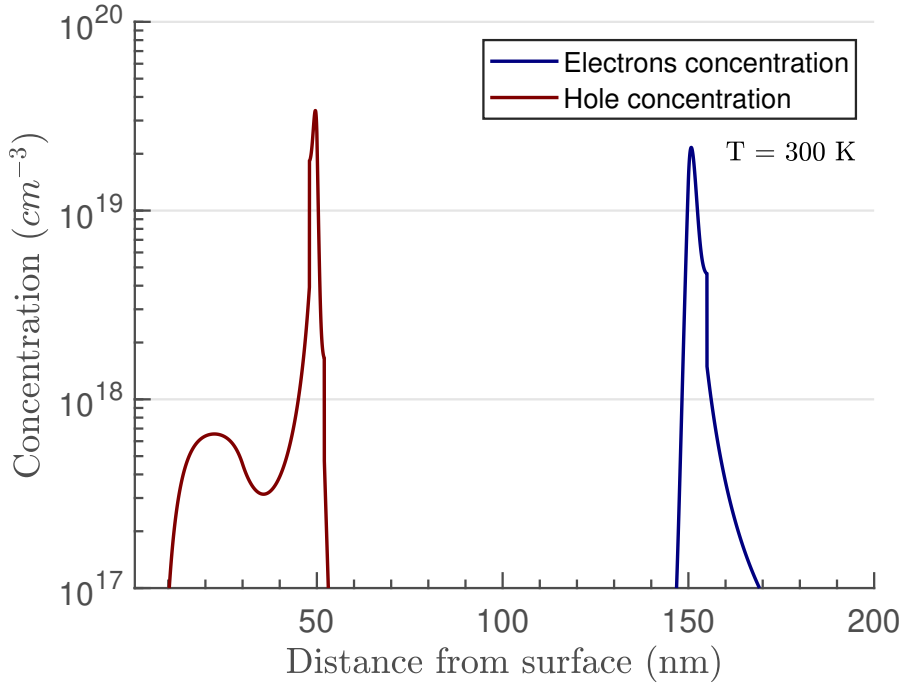


Figure 3.3: Electron and Hole concentration of pGaN-GaN-AlGaN-GaN structure

In order to validate the accuracy of Nextnano, a comparison with Nakajima et al. work has been done. In this work [24], Nextano was also used to simulate a double-heterojunction, of which in later works [25, 23], the sheet hole and electron density were confirmed through hall-measurements. During the simulations in this thesis, the structure inputs have been validated using Nakajima's work to validate the used settings in Nextnano.

Due to the direct use of Nextnano's outputs in the simulation steps to estimate the Seebeck coefficient and electrical conductivity, Nextnano is also included indirectly in both simulation models' validation process. Both the Seebeck-coefficient and conductivity models will be verified using state-of-art structures that require a simulation step to determine both the structure's electron density and energy levels, which are simulated and provided by Nextnano.

3.2. Electrical mobility and conductivity model

The formation of a 2DHG provides the opportunity to create a conductive layer that forms without local dopants to create free holes. This section describes the method used to simulate a 2DHG mobility by individually assessing the scattering mechanisms affecting the mobility.

3.2.1. Average scattering time and mobility

The mobility of holes and electrons can be expressed using Equation 3.1, depending on the effective mass m*, elementary charge e, and the average scattering-time $<\tau>$ of the carriers.

$$\mu = \frac{e}{m*} <\tau> \tag{3.1}$$

The total scattering time $\tau(E)$ is calculated by taking the sum of individual scattering components as a function of energy, as seen in Equation 3.2. To determine the average scattering time $<\tau>$, the energy-dependent total scattering is averaged using Fermi statistics as seen in Equation 3.3, where f_0 is the Fermi function and $\tau(E)$ the earlier found energy-dependent total scattering time.

$$\tau(E) = \sum (\tau_j^{-1}(E))^{-1} \tag{3.2}$$

$$<\tau>= \frac{\int \tau(E) E \frac{\delta f_0(E)}{\delta E} dE}{\int E \frac{\delta f_0(E)}{\delta E} dE} \tag{3.3}$$

3.2.2. Energy dependent scattering in 2-Dimensional inversion layer

A total energy-dependent scattering time model can be simulated by individually determining the different scattering processes within a 2DHG. To analytically express the energy-dependent scattering mechanisms, the energy levels of a 2DHG are extracted from the Schrödinger-Poisson solver.

The electron energy is expressed using Equation 3.4 where E_n is the bottom of the corresponding subband where most free electrons are located. The bottom of this subband is extracted from the earlier mentioned Schrödinger-Poisson solver to include changes to E_n over Temperature and other structural changes. This method introduces the direct relation between the Schrödinger-Poisson solver and estimated mobility, reducing the need for approximations to determine energy levels using the carrier density. This proposed method determines the hole mobility by extracting the bottom of the valence band and the hole density.

$$E_n(k) = E_n + \frac{\overline{h}^2 k^2}{2m*} \tag{3.4}$$

Further, to determine the 2-dimensional scattering mechanisms, the 2D screening effect is introduced by dividing the scattering matrix elements by the screening function S(q,T) as seen in Equation 3.5 where F(q) is the form factor, further explained by Hirakawa [15] and $\Pi(q,T,E)$ the polarizability function seen in Equation 3.6, where Θ is the unit-step function, K_F the Fermi-wave vector, E_F the Fermi-energy extracted from Nextnano, and T the Temperature in Kelvin. The Fermi-wave vector is further estimated using Equation 3.7 where h_{2D} is extracted from Nextnano.

$$S(q,T) = 1 + \frac{e^2 F(q) \Pi(q,T,E)}{2\epsilon q} \tag{3.5}$$

$$\Pi(q,T,E) = \frac{m*}{4\pi \overline{h}^2 k_B T} \int_0^\infty \frac{1 - \Theta(q - 2K_F)[1 - (2K_F/q)^2)]^{1/2}}{cosh^2[(E_F - E)/2k_B T]} dE \tag{3.6}$$

$$K_F = \sqrt{2\pi h_{2D}} \tag{3.7}$$

3.2.3. Scattering mechanisms

By applying the aforementioned 2D screening effect, the scattering mechanisms present in the formed QW are now investigated. The scattering mechanisms considered in the model are deformation scattering, potential scattering, surface roughness scattering, and optical phonon scattering. Ionized impurity scattering is neglected since the AlGaN barrier layer is considered not doped. Furthermore, piezoelectric scattering is ignored, as it is negligible [13].

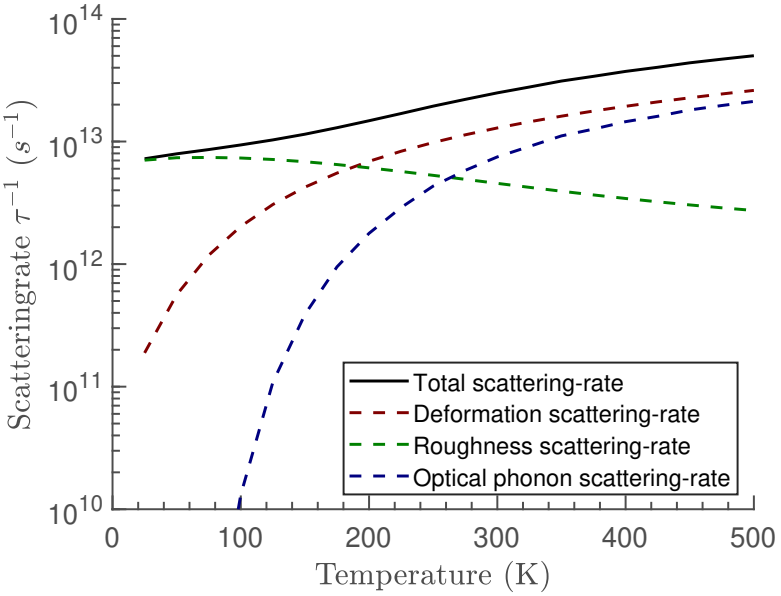


Figure 3.4: Scattering-rate of individual mechanisms in 2DHG of Sample A shown in Table 3.1 over range of temperatures

Based on earlier work [13], the interface roughness scattering τ_{ir} can be expressed using Equation 3.8. The integral over θ is taken from 0 to 2π, with the process-dependent statistical variables Δ and λ representing the interface's average displacement and autocorrelation length, respectively. Both variables are determined experimentally using X-Ray Diffraction (XRD) measurements and are assumed to have a Gaussian distribution. Furthermore, ϵ represents the dielectric constant of GaN, and n_{2D} represents the electron or hole density.

$$\tau_{ir}^{-1} = \frac{m^*(\Delta\lambda)^2}{2\overline{h}^3}\int_\theta exp(-\frac{q^2\lambda^2}{4})[\frac{(e^2/\epsilon)(n_{2D}/2)}{S(q,T)}]^2(1-cos(\theta))d\theta \tag{3.8}$$

Deformation scattering, commonly known as acoustic phonon scattering, can be expressed using Equation 3.9[13]. Where the integral is taken from 0 to 2π, E_{dp} is the deformation potential and C_L the longitudinal elastic constant of GaN

$$\tau_{dp}^{-1} = \frac{3bE_{dp}^2 m^* k_B T}{32\pi\overline{h}^3 C_L}\int_\theta \frac{(1-cos(\theta))}{S^2(q,T)}d\theta \tag{3.9}$$

Optical phonon scattering can be expressed using Equation 3.10[13]. With ω_{LO} the longitudinal optical phonon energy, ϵ_∞ the optical or high-frequency dielectric constant. $q_{||+}$ and $q_{||-}$ represent the scattering wave vectors in absorption and emission and N_q the phonon occupation number, further explained by Gurusinghe [13].

$$\begin{aligned}\tau_{po}^{-1} = \frac{e^2 m^* \overline{h}\omega_{LO}(\epsilon_\infty^{-1}-\epsilon^{-1})}{8\pi^2\overline{h}^3[1-f_o(E)]}\int_0^{2\pi}(1-cos(\theta))\{&[1-f_o(E+\overline{h}\omega_{LO})]N_q I(q_{||+})+\\ &[1-f_o(E-\overline{h}\omega_{LO})]\Theta(E-\overline{h}\omega_{LO})(N_q+1)I(q_{||-})\}d\theta\end{aligned} \tag{3.10}$$

To better understand the individual contribution of the scattering mechanisms that limit the hole mobility over different temperatures, a plot of the scattering rates over the temperature of the individual mechanism is provided in Figure 3.4. By each comparing the scattering mechanisms, it can be stated that in cold environments of 200 Kelvin and below, the total scattering rate is mainly influenced by surface roughness scattering. In contrast, acoustic and optical phonon scattering are dominant in higher temperatures. Both phonon scattering mechanisms are primarily bound by material-dependent variables and, therefore, are hard to improve. Whereas the surface roughness can be improved using different MOCVD techniques. As a result, further technology improvements will be primarily seen in low-temperature performance.

In conclusion, the scattering rate decreases with temperature, resulting in higher hole mobility in low-temperature environments. This decrease improves the power factor of a GaN based TEG in lower temperatures.

3.2.4. Model validation using state-of-the-art

With the now fully defined model, it is necessary to verify the accuracy of the estimation using earlier measurements from state-of-the-art structures. The earlier introduced p-GaN-GaN-AlGaN-GaN structure has been characterized by Nakajima [23], in which the hall-mobility is measured over a temperature range of 25 to 500 Kelvin. During the characterization of this structure, two different structure thickness variations are measured and compared, listed in Table 3.1 and can be represented with the earlier introduced 2-dimensional cross section in Figure 2.6. Both samples are individually simulated using the proposed simulation method introduced above.

Sample:	p-GaN thickness	GaN thickness	AlGaN thickness	Al content
A[23]	30 nm	20 nm	48 nm	23 %
B[23]	30 nm	60 nm	47 nm	23 %

Table 3.1: Sample overview mobility experimental measurement and simulation comparison

Firstly, the structure is simulated in Nextnano to obtain the necessary intermediate results regarding sheet density and energy levels. These intermediate results are then used to estimate the mobility of a 2DHG. This process is carried out over a temperature range similar to Nakajima's results to provide a dataset comparable to their measurement results. This method results in Figure 3.5, where the simulation and state-of-the-art measurement results can be compared.

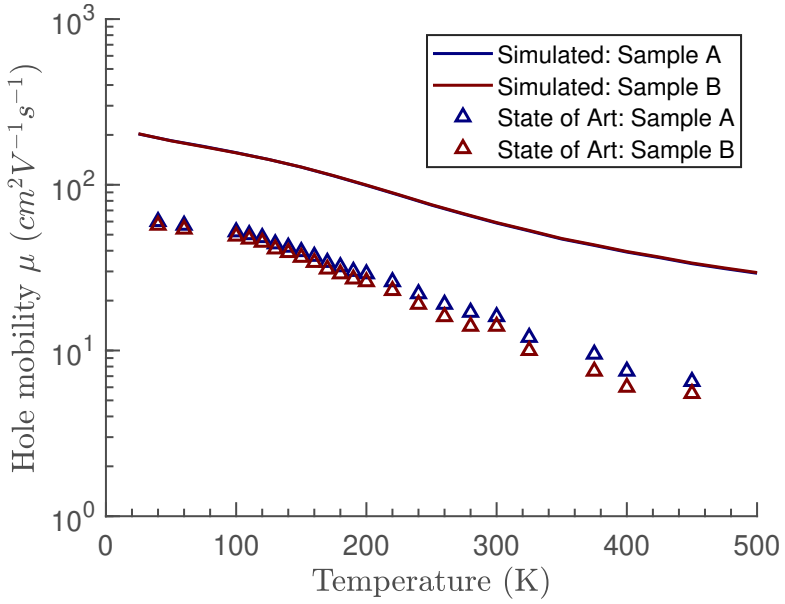


Figure 3.5: Simulation and state-of-art measurement results of 2DHG mobility

As seen from Figure 3.5, a discrepancy between the simulated and state-of-the-art measurements can be noted of half an order of magnitude. This discrepancy is most likely due to unknown variables for the simulation, such as the surface roughness constant on the heterojunction and the absence of the simulated unintentional dopants in the channel. Furthermore, apart from a constant error, the general behavior of the simulated mobility over the temperature range does coincide with the state-of-the-art behavior measured by Nakajima et al. [23].

As stated by Nakajima et al.[23] as part of their studies, the difference between samples A and B is minimal. As seen in both the performed simulations and state-of-the-art measurements, further increasing the confidence of the simulation model for further evaluations of 2DHG structures.

3.3. Seebeck coefficient model

The complete model introduced in Figure 3.1 separately simulates the Seebeck coefficient as one of its intermediate steps. The earlier stated formula for the Seebeck coefficient, Equation 2.10 in the background of this thesis, has been used to determine the Seebeck coefficient of 2DHG quantum wells in state-of-the-art works. This work introduces a novel method to calculate the Seebeck coefficient using the earlier found energy levels from the Schrödinger-Poisson solver.

As mentioned in subsection 2.2.1, the distance between the Fermi-level (E_F) and Valence-band (E_V) is an important metric to determine the Seebeck-coefficient of a 2DHG. Conventional methods determine the Valence-band energy levels by applying the known hole density to the density of states. The density of states provides a fast method to analyze the structure's energy levels but introduces uncertainty since it simplifies the energy levels.

In this work, the earlier calculated energy levels of the QW are extracted from the Schrödinger-Poisson solver instead of estimating the energy levels using the density of states. This newly introduced method introduces a direct coupling between the Seebeck coefficient and the earlier simulated structures' energy levels.

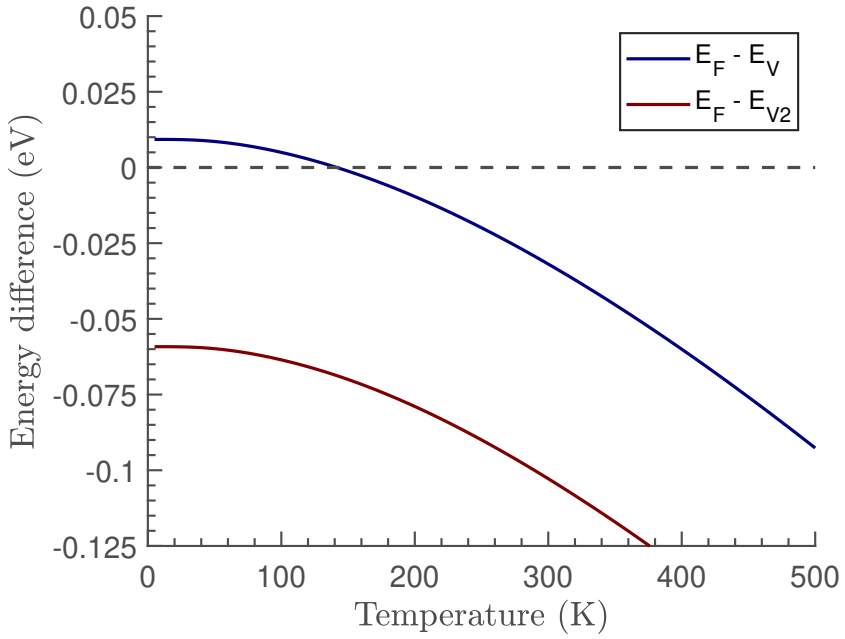


Figure 3.6: EF - EV1 over different temperatures

The Schrödinger-Poisson solver outputs multiple valence bands in its simulation results, contributing to the overall hole population. However, this analysis focuses on the top valence band, as it contains the majority (> 90 %)of the holes in the QW. This method simplifies the Seebeck-coefficient calculations.

Figure 3.6 shows the top valence band location with the Fermi level over a wide temperature range. This change of energy difference over temperature is typically not considered as detailed when estimating the energy difference using the sheet density and density of states. Therefore, using the direct results of the energy-based simulations of Nextnano in the Seebeck-coefficient model is expected to improve the estimation of the Seebeck-coefficient.

$$\begin{aligned} S &= -\frac{1}{qT}\frac{\int_0^\infty \sigma(E)(E - E_F - E_{V1})dE}{\int_0^\infty \sigma(E)dE} \\ &= -\frac{1}{qT}\frac{\int_0^\infty E\cdot\tau(E)\frac{\delta f_0}{\delta E}(E - E_F - E_{V1})dE}{\int_0^\infty E\cdot\tau(E)\frac{\delta f_0}{\delta E}dE} \end{aligned} \tag{3.11}$$

With the newly established method of importing simulated energy levels and the earlier established conductivity of a 2DHG. A simplified yet improved equation for the Seebeck coefficient is used. Equation 3.11 is used to calculate the Seebeck coefficient with the energy level difference between the Fermi-

level and Valence band, including the differential conductivity of the QW represented by $E \cdot \tau(E)\frac{\delta f_0}{\delta E}$, earlier extracted from the mobility simulations in section 3.2 where $\frac{\delta f_0}{\delta E}$ represents the derivative of the Fermi-Dirac function. Furthermore, q represents the charge-carrier charge, and T is the average temperature of the semiconductor.

3.3.1. Model validation using state-of-the-art

A comparison with state-of-the-art measurement data must be carried out to validate the simulation model explained above. Since no state-of-the-art data is available on GaN based 2DHG Seebeck coefficients, other data must be used to validate the newly introduced model. Former, earlier mentioned, research of A. Yalamarthy et al. [29] and C. Bryan et al. [7] in which the Seebeck coefficient of GaN 2DEGs is measured for different GaN thicknesses is used to validate the newly introduced model. Changing the newly set up model for n-type quantum wells and simulating the structures used by both researchers can compare the simulation and measurement data as seen in Figure 3.7.

When comparing the simulation data with their respectable state-of-the-art measurements, it is necessary to address each sample, as each sample shows significantly different results. The list of samples used to compare to the state-of-the-art measurement and simulation is given in Table 3.2.

Sample	Layer 1 (Top)	Layer 2	Layer 3	Layer 4	Layer 5	Layer 6
A [29]	3 nm u-GaN Cap	30 nm AlGaN x = 0,25	1 nm AlN	100 nm u-GaN 2DEG Channel	Buffer	Si
B [29]	3 nm u-GaN Cap	30 nm AlGaN x = 0,25	1nm AlN	1.2 um u-GaN 2DEG channel	Buffer	Si
C [7]	5 nm SiN Cap	25 nm AlGaN x = 0,218	0.7 nm AlN	100 nm u-GaN 2DEG channel	Buffer + AlN	Si

Table 3.2

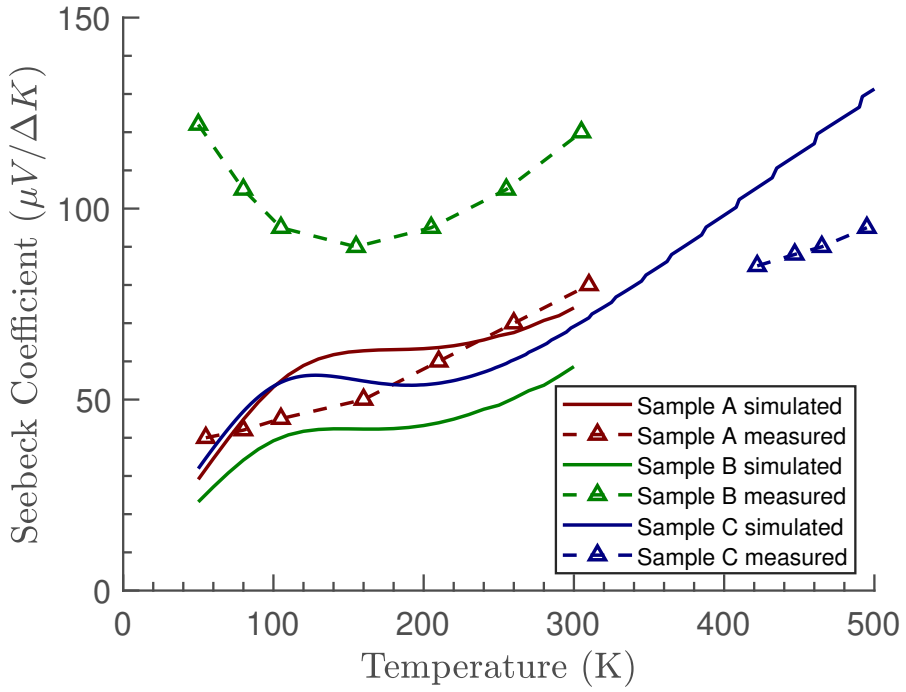


Figure 3.7: Seebeck coefficient simulation and state-of-the-art measurements of 2DEG channels of different samples a seen in Table 3.2

Firstly, Yalamarthy's 'thin' sample (A) shows the most similarity between the simulations and measurement data. This similarity is expected as the simulation model is optimized for structures such as

the thin GaN structure proposed by Yalamarthy. The order of magnitude and curvature prove that the simulations represent the measured realized samples.

However, Yalamarthy's second 'Thick' sample is not entirely similar when comparing the simulation data with the measured data, especially in the lower temperature range. This result was expected, as this structure is optimized to benefit from phonon-drag, boosting the overall Seebeck coefficient. This additional phonon-drag improvement of the Seebeck coefficient is absent in the simulations, resulting in a discrepancy between the simulation and measurement data. As seen in Figure 3.7, in sub-100 Kelvin temperatures, the simulated Seebeck coefficient is significantly lower than the measurement data. This phonon-drag phenomenon is considered out-of-scope and is not expected to be present in the structures of interest in this work.

C. Bryan's [7] measurement results are focused on above 400 Kelvin measurements. Comparing the simulated Seebeck coefficient with the measured data, it can be stated that a further increase in the Seebeck coefficient is seen in the simulated and measured data. However, a drift error can be observed as the temperatures increase, stating that this simulation model is mostly reliable in temperatures up to 500 Kelvin.

Both sample A and C's simulation results show a local maximum at 125 Kelvin, which is mostly caused by the difference between the Fermi-level and valence band to be close to zero, which can be seen in Figure 3.6. This local maximum is only observable in simulation results and is not observed as pronounced in state-of-the-art measurements. This local maximum, therefore, should be considered as a simulation artifact that can be disregarded. Apart from the local maximum at 125 Kelvin, the trend of the simulation does match the state-of-the-art measurements as mentioned above.

In conclusion, the proposed Seebeck coefficient simulation model can reliably predict the performance of 2DEG based simulations as long as there is limited phonon drag in low temperatures. The model can predict the Seebeck coefficient for temperatures up to 300 Kelvin, when disregarding local maxima due to $E_F - E_V$ crossing zero.

3.4. Thermal conductance

The thermoelectric properties of materials used in TEGs provide a first indication of the performance of different materials. The thermal conductance of a material used in a TEG is directly related to the device's efficiency, as the thermal conductivity is related to the heat flux within the structure. The efficiency of a complete TEG comprised of intricate structures depends on the rate heat conducts through the used materials. Thermal leakage is considered lost energy in the form of heat and can be estimated using the thermal conductivity of the materials the TEG is made of. Since this thesis is focused on forming a confined 2DHG layer in a multi-material stack-up, the thermal conductance of this stack-up is estimated using a numerical model, as explained below.

3.4.1. Overall thermal conductance of stack-up

As stated above, the formation of a 2DHG is realized by creating a stack of multiple different epitaxially grown layers of GaN, AlGaN, and possibly other materials. Since these materials differ in their thickness and characteristics, the overall thermal conductivity of the complete stack is estimated by taking the sum of the thermal conductivity of each layer, weighted by their thickness as seen in Equation 3.12. This weighted average thermal conductivity of the stack-up provides a proven effective method [35] to estimate the overall thermal conductance of a stack-up that is compatible with Finite Element Method (FEM) simulation software, allowing simulating more complex TEG structures.

$$k_{tot} = \frac{\sum k_i \cdot t_i}{\sum t_i} \tag{3.12}$$

3.4.2. Thermal conductance of single layers

In order to calculate the stack-up's overall thermal conductivity, each layer's thermal conductance is estimated separately. The thermal conductivity of crystalline materials such as GaN, AlGaN, or metals comprises the heat carried by electrons and phonons and can be formulated as $k_i = k_e + k_p$. The contribution of electrons to the thermal conductance in semiconductors is negligible as the number of free electrons is insignificant[12]. Therefore, modeling the thermal conductance of lattice vibrations, commonly known as phonons, is sufficient for an approximation of the thermal conduction of each layer.

The thermal conductance through lattice vibrations can be expressed using Equation 3.13, based on the BTE model, where the specific heat capacity $C(\omega)$, the specific velocity $v(\omega)$ and the mean free path $\lambda(\omega)$ of different phonon modes are integrated. A summation is taken to include the two transverse phonon modes and one longitudinal phonon mode for more general cases.

$$k_p = \sum_{LA,TA} \frac{1}{3} \int C(\omega) v(\omega) \lambda(\omega) d\omega \tag{3.13}$$

The mean free path $\lambda(\omega)$ can be estimated in the form of phonon scattering $\tau(w)$ multiplied by the phonon velocity $v(\omega)$, resulting in Equation 3.14.

$$k_p = \sum_{LA,TA} \frac{1}{3} \int C(\omega) (v(\omega))^2 \tau(\omega) d\omega \tag{3.14}$$

The in-plane thermal conductivity can be further approximated using the Debye approximation, in which one single acoustic band is assumed with an average phonon velocity v_{av} overall phonon modes. By taking $x = \overline{h}\omega/(k_B T)$ in combination with the Debye approximation, the in-plane conductivity can be estimated using Equation 3.15 [32] in which Θ_D is the material dependent Debye temperature.

$$k_i = \frac{k_B^4 T^3}{2\pi^2 \overline{h}^3 v_{av}} \int_0^{\theta_D/T} \frac{x^4 e^x \tau(x)}{(e^x - 1)^2} dx \tag{3.15}$$

3.4.3. Phonon scattering

The equation above shows that the total phonon scattering time τ determines the in-plane thermal conductivity. The total phonon scattering time is determined using Matthiessen's rule, in which different scattering mechanisms within the material are considered. Firstly, phonon-phonon scattering is evaluated using the Umklapp process, where N-phonon interactions change the net direction of phonon

propagation within a medium. The Umklapp-process scattering time can be approximated using Equation 3.16 [39], where P and Cu are material-dependent constants.

$$\tau_U(x) = \frac{P k_B^2 T^3 x^2 e^{\frac{-C_U}{T}}}{\overline{h}^2} \tag{3.16}$$

Defect scattering in the form of core defect, screw defect, edge defect, and mixed dislocations is included in the total scattering term. The scattering time of the defects is approximated with the total dislocation density N_{dis}, which represents the total process-dependent dislocations of the deposited layer. As the core, screw, edge, and mixed dislocation scattering approximations are all dependent on different material parameters, except the shared dislocation density, it can be noted that the dislocation scattering time is inversely proportional to the dislocation density. This concludes that the defect scattering time decreases as the dislocation density increases. In experimental results, the dislocation density N_{dis} is typically extracted using XRD measurements. The phonon-dislocation scattering is approximated using the approach proposed by Zou et al. [40].

Boundary scattering is commonly known as the interaction between phonons and the boundaries of a thin film layer, reducing the heat conductivity of a material due to phonons interacting with boundaries in a layered structure. Boundary scattering heavily depends on the layer thickness as boundary scattering becomes more noticeable in thin films[21, 39]. The boundary scattering term can be estimated using Equation 3.17, in which the thickness of the layer t_i and average phonon velocity v_{av} are considered with a dimensionless scalar of 2.38, this approach is commonly found in nanowire models and is experimentally acquired and verified for GaN and AlGaN layers[39, 5].

$$\tau_B \approx \frac{2.38 t_i}{v_{av}} \tag{3.17}$$

Phonon-impurity scattering is neglected in this thermal conductivity model as impurity scattering is negligible in unintentionally doped GaN and AlGaN[5].

3.4.4. Results

By applying the in-plane thermal conductivity models as shown here, a structured method can be determined to calculate the total thermal conductance of the stack-up. The resulting model shows a heavy dependency on the thickness of each layer, as phonon-surface scattering is considered the most dominant scattering mechanism in thin films. Since the stack-up used in this thesis is mainly comprised of deposited thin films, the thermal conductivity is expected to be relatively low ($80 \frac{W}{m \cdot K}$), improving the efficiency of the TEG. This model has not been validated as it is not considered for PF optimization of 2DHGs. The model can, however, be used for the final validation of the Figure of Merit (FoM) of just the 2DHG channel alone in future works.

3.5. Structure optimization for 2DHG TEGs Power Factor

With the complete simulation stack as suggested in Figure 3.1 now validated with the help of state-of-the-art measurement data, the performance of different GaN 2DHG structures can be compared. The optimization of a 2DHG structures is aimed to determine the structure with the maximum resulting Power Factor (PF) over different functioning temperatures. This result will give an insight into the performance of optimized structures over various temperature ranges to compare with state-of-the-art TEG materials. It will determine the structure(s) that will be realized for further measurements.

During the optimization process, multiple structure variables are investigated. As mentioned earlier in the background, this thesis is mainly based on a polarizing structure earlier introduced by Nakajima [25] which can be seen in Figure 2.5. During the optimization process, the 2DHG density is firstly investigated and optimized before the PF. During this process, the top two layers' optimal thickness is optimized, as seen in subsection 3.5.1. With a now optimized top two layers, the polarizing AlGaN layer is thoroughly simulated for different thicknesses and Aluminum content levels to investigate the hole-density range achievable with the proposed structure in subsection 3.5.2. With a now defined range of possible hole-densities as a function of the polarizing AlGaN layers properties, the PF can be determined with the help of the complete simulation model proposed in chapter 3.

3.5.1. Mg doped GaN surface charge depletion

To form a high mobility 2DHG channel in the u-GaN channel, a Mg-doped GaN layer on the surface is required to minimize surface charge-depletion by adding an opposing charge in the p-GaN top layer. This surface-depleting p-GaN layer positively influences the hole density of the formed 2DHG at the cost of a thicker structure with higher thermal conductivity and cost. Therefore, an optimum can be found by simulating a structure with varying p-GaN thicknesses and comparing the hole density for an optimum result.

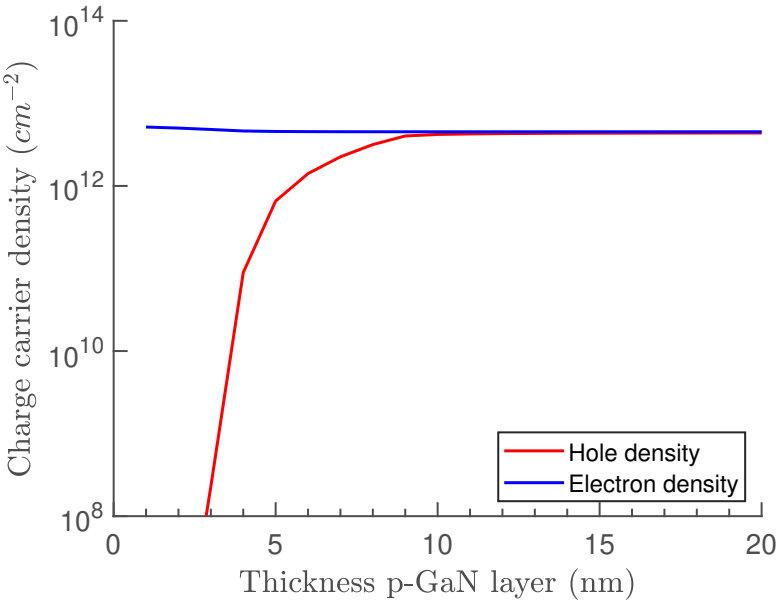


Figure 3.8: 2DHG and 2DEG sheet density over p-GaN thickness with constant 20 nm u-GaN, an AlGaN thickness of 40 nm and Aluminum content of 20%

In Figure 3.8, a performed sweep simulation of said p-GaN thickness is seen, in which the hole and electron density are plotted of the 2DHG and 2DEG respectively. As can be seen in the figure, the electron density is independent of the p-GaN layer. In contrast, the hole density heavily depends on a minimal thickness of 10 nm and saturates at a density closely matching that of the electron gas. Therefore, a minimal p-GaN thickness of 10 nm must be chosen for an optimal result. For a reliable result in which a uniform layer with no island forming can be deposited, a thickness of 30 nm is determined. During these simulations, a constant Mg doping level of $3 \cdot 10^{19} cm^{-3}$ has been chosen, based on the maximal practical and achievable density according to Kumar et al. [19]

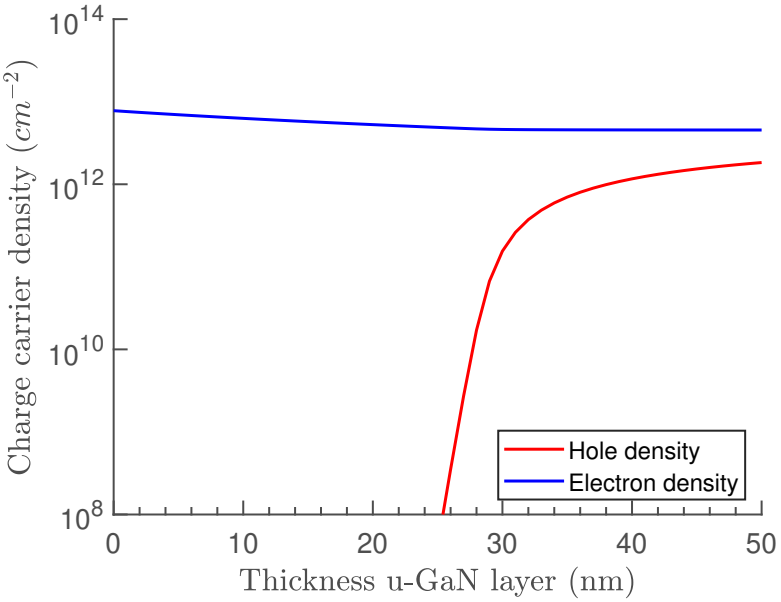


Figure 3.9: 2DHG and 2DEG sheet density over u-GaN channel thickness with no p-GaN deposition, an AlGaN thickness of 40 nm and Aluminum content of 20%

Another approach in which no p-GaN layer is used is investigated by significantly increasing the thickness of the unintentionally doped GaN layer in which a 2DHG forms. As seen in Figure 3.9, the hole density is plotted as a function of the GaN channel thickness. The hole density starts saturating at a thickness of 30 nm, with a significant decrease in hole density compared to the earlier proposed method in which a p-GaN layer is used to overcome this issue.

In conclusion, two different methods of surface depletion have been investigated where a significant improvement can be found by using a p-GaN layer on top of the unintentionally doped GaN layer. A final layer thickness of the p-GaN layer of 30 nm is chosen for further simulations of the 2DHG structure.

3.5.2. Hole density as a function of AlGaN layer properties

As introduced in subsection 2.4.2, the hole density is controlled by strain subjected by the AlGaN layer onto the GaN layers due to lattice mismatch. Increasing the aluminum content, commonly denoted as x, increases the electron and hole density significantly. This relation is simulated by the Schrodinger-Poisson solver. It can be used to determine the ideal PF as the sheet density of the holes directly alters the structure's performance. The thickness of the AlGaN layer is as crucial since it also increases the polarizing effect through the piezoelectric properties of the structure.

By sweeping the AlGaN aluminum content for different thicknesses, a range of hole sheet densities can be determined and plotted, as seen in Figure 3.10.

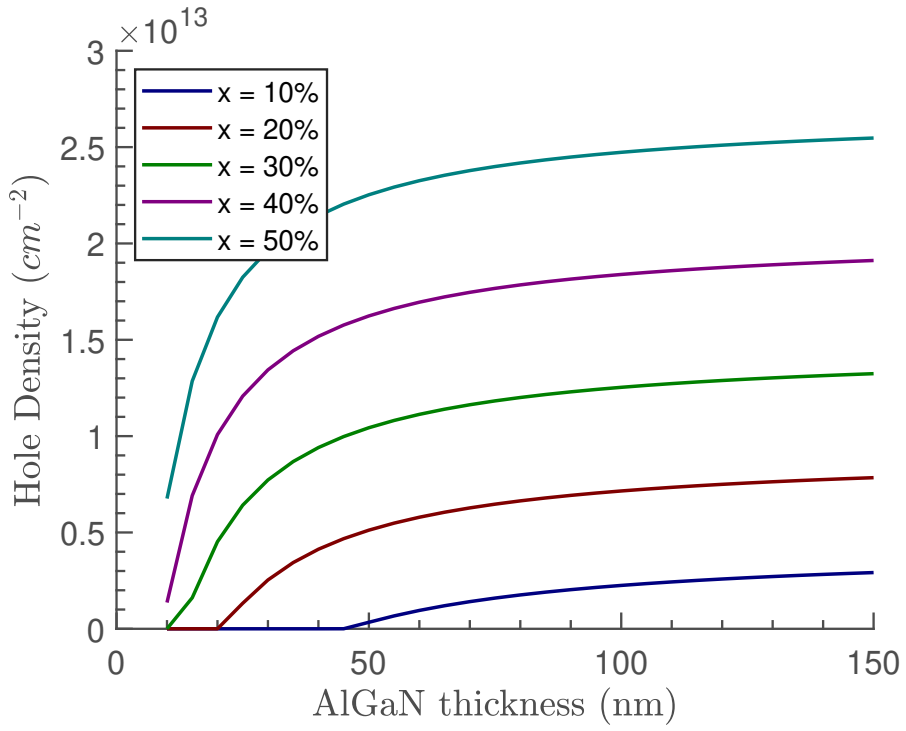


Figure 3.10: Hole density, with varying AlGaN thickness and aluminum content at room temperature

Figure 3.10 shows a stable region of interest for any aluminum content percentage with a AlGaN thickness of 50 nm and above. All structures with an AlGaN thickness below 50 nm show a diminishing hole density as a result of the minimal polarizing effect of the AlGaN/GaN heterostructure mismatch. Therefore, to reliably induce a 2DHG, it is required to have a minimal AlGaN thickness of 50 nm.

By comparing the differently colored lines in Figure 3.10, a better understanding of the effect of aluminum content within the AlGaN can be provided. As seen in the figure and stated before, a thickness of 50 nm or higher is required for any of the aluminum contents. A key difference is the hole density in the stable region, where an increased aluminum content results in a higher hole density. This relation between the aluminum content and hole density was as expected and provides the opportunity to select a hole density in the range of $1 \cdot 10^{12} - 3 \cdot 10^{13} cm^{-2}$.

An optimal structure can be found by taking the simulation results from the Schrödinger-Poisson solver and estimating the Seebeck coefficient and mobility of the structures with different aluminum content and AlGaN thicknesses.

3.5.3. Seebeck coefficient, Conductivity and Power Factor as a function of hole density

The Seebeck coefficient and mobility are initially simulated to determine the PF. By taking the earlier simulated structure sweeps where the aluminum content and AlGaN thickness are varied, a variety of structures with a hole density between $1 \cdot 10^{12} - 3 \cdot 10^{13} cm^{-2}$ is taken for further evaluation.

The structures used above with varying AlGaN thickness and aluminum content are used to run the conductivity and Seebeck coefficient estimations to include the complete range of hole densities. As can be seen in Figure 3.11, where each structure sweep is simulated for different temperatures, many lines are seen. Each line is considered a sweep, where multiple structures are simulated at the same temperature.

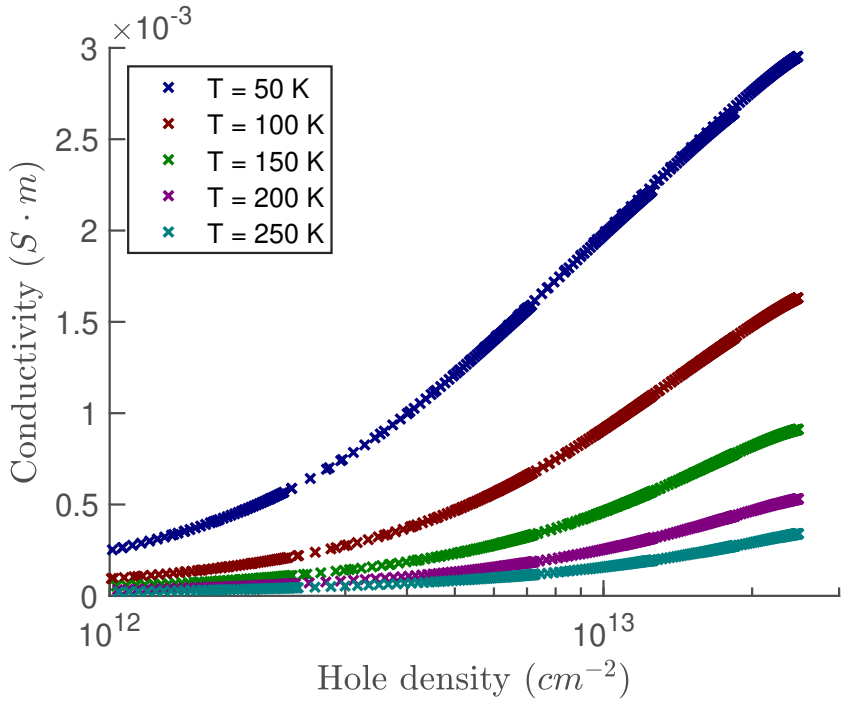


Figure 3.11: Conductivity of the formed 2DHG with different hole densities

Figure 3.11 plots the calculated conductivity as a function of Hole density, which was estimated by simulating the structures mentioned above using the proposed simulation method in section 3.2. As expected, a positive correlation between the sheet hole density and conductivity can be noted. Whereas an apparent decrease of conductivity is seen as the temperature increases due to the rise of scattering within the QW with the increase in temperature as noted in section 3.2

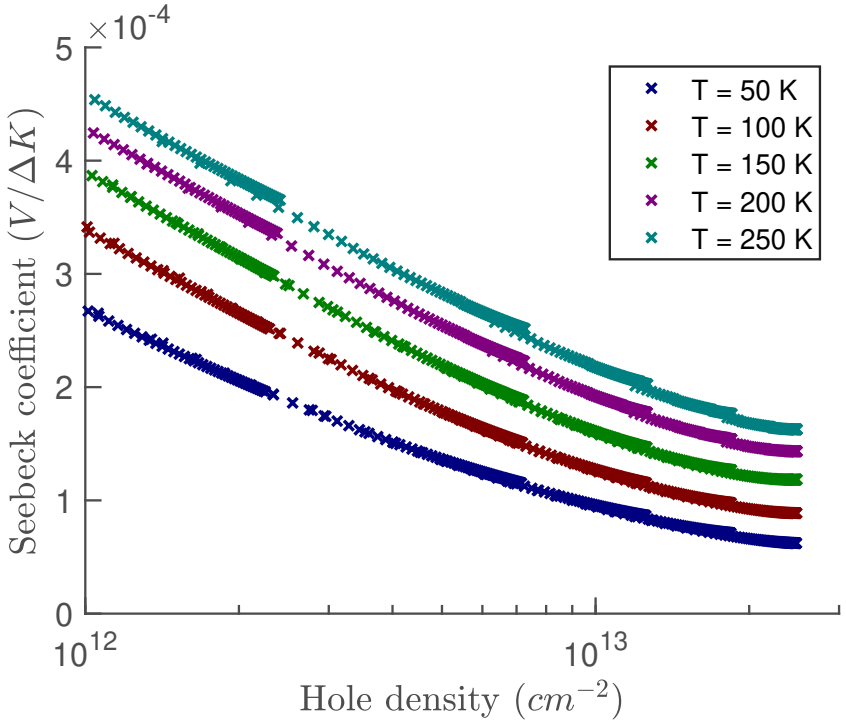


Figure 3.12: Seebeck coefficient of the formed 2DHG with different hole densities

As a result, a similar method is used to calculate the Seebeck coefficient, with Figure 3.12. From

this plot, the clear conclusion can be taken that, as expected, the Seebeck coefficient significantly decreases with an increase in the sheet hole density. A correlation between the temperature and the Seebeck coefficient can also be noted, in which an apparent decrease in the Seebeck coefficient is seen for lower temperatures.

With the now estimated Seebeck coefficient and conductivity of a 2DHG, the power factor of the complete setup can be determined over different sheet hole densities. The power factor is calculated using Equation 3.18 for each individually simulated structure.

$$PF = S^2\sigma \tag{3.18}$$

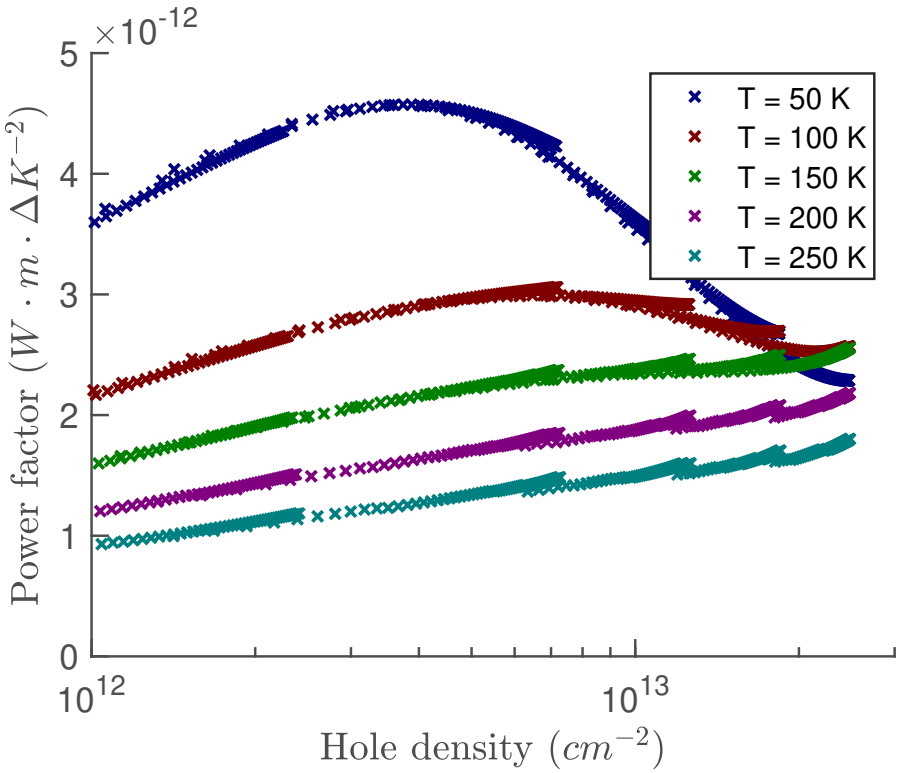


Figure 3.13: Power Factor of the formed 2DHG with different hole densities

Figure 3.13 plots the simulated PF as a function of hole density for multiple temperatures. From this graph, it can be noted that a clear increase in the PF can be seen for lower temperatures, concluding that the conductivity of the 2DHG is a dominant influence on the overall performance of the proposed structure. Another noticeable difference between the different temperatures is the maximum PF shifting towards higher hole sheet densities. For temperatures of 200 Kelvin and above, the maximum PF is observed to exceed the currently possible hole sheet density available.

3.6. Proposed structures and expected performance

With a clear insight into the maximum PF over different temperatures and hole densities, a decision can be made to determine the ideal GaN stack-up. To confirm the simulated PF over different hole densities, it is recommended to realize multiple wafers with differing AlGaN properties. As a result, a list of five wafer stack-ups is proposed for further investigation. Table 3.3 provides five different stack-ups, properly covering the sheet hole density.

Sample:	p-GaN thickness	GaN thickness	AlGaN thickness	Al content	Sheet Hole Density @ 50K
A	30 nm	20 nm	100 nm	10 %	$0.2 \cdot 10^{13}\ cm^{-2}$
B	30 nm	20 nm	100 nm	20 %	$0.7 \cdot 10^{13}\ cm^{-2}$
C	30 nm	20 nm	100 nm	30 %	$1.2 \cdot 10^{13}\ cm^{-2}$
D	30 nm	20 nm	100 nm	40 %	$1.7 \cdot 10^{13}\ cm^{-2}$
E	30 nm	20 nm	100 nm	50 %	$2.5 \cdot 10^{13}\ cm^{-2}$

Table 3.3: Sample overview mobility experimental measurement and simulation comparison

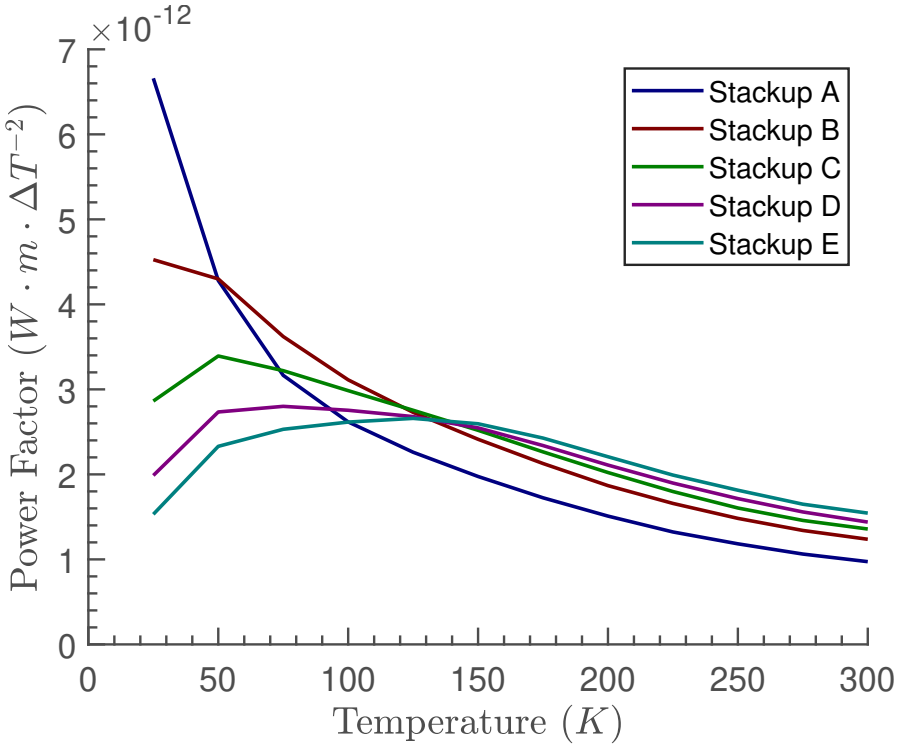


Figure 3.14: Power Factor of proposed structures, showing the converging point at 125 Kelvin

Simulating the proposed stack-ups and comparing their resulting PF over a varying temperature, as seen in Figure 3.14, a point of convergence is noted around 125 Kelvin. This point of interest marks the temperature at which the optimization strategy significantly changes. Where below 125 Kelvin, the stack-up with the lowest sheet hole density outperforms the higher sheet density stack-ups. In addition, the optimal power factor moves to lower temperatures as the sheet hole density decreases. It can be noted that in higher temperature ranges, the difference between the individual stack-ups becomes indistinguishable.

3.7. Conclusion

This chapter introduced a novel method of simulating GaN 2DHGs, which has been verified using state-of-the-art measurement data of different structures to determine the reliability of said models. The verified models determine the sheet hole density, Seebeck coefficient, electrical conductivity, thermal conductivity, and the Power Factor of the 2DHG for different AlGaN thicknesses and aluminum contents. The simulated PF has been compared to determine a range of interest for experimental measurements with a point of interest in which the optimization strategy drastically changes over different temperature ranges.

With the help of the now simulated range of interest, a wafer can be realized to prove the presence of said 2DHG and measure the performance mentioned above metrics.

4

GaN 2DHG realization and fabrication

To carry out measurements to compare to the earlier simulations, a GaN wafer must be specified, acquired, and prepared for measurements. This chapter provides a detailed overview of the steps taken to determine the GaN die sizes, and the fabrication process used to prepare the GaN dies.

Firstly, the Device Under Test (DUT) is determined in section 4.1, including a printed circuit board (PCB) design in combination with a method to determine the width and length of the GaN dies. After the die size and PCB has been designed, the GaN on Silicon (Si) structure is chosen and realized in section 4.2. To carry out measurements and verify the usability of GaN structures, the electrical connectivity to the 2DHG is discussed in section 4.3. To realize the Ohmic contacts, the fabrication process is described in section 4.4, including some intermediate fabrication results.

4.1. Devices under test, die size determination and measurement PCB design

To reliably measure the Seebeck coefficient, a PCB must be realized, creating a thermal gradient over a strip of GaN and providing a method to contact the metal surfaces on the dies for measurements. Additionally, a PCB is desired to bond the metal contacts of a 4-pt sheet resistance measurement. Therefore, a single PCB is designed to fulfill both measurement needs simultaneously.

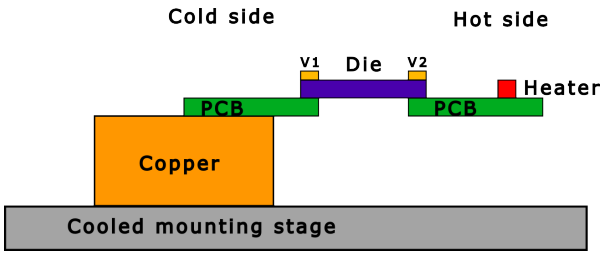


Figure 4.1: Illustration of Diving-board (not to scale)

A proposed ”diving plank” model is shown in Figure 4.1. This test structure is designed to mount a long strip of GaN and thermally connect it to each side of the PCB. One end of the PCB is connected directly to the cryogenic cooler through a copper block, making it the cold side. The other side of the PCB contains resistors to heat the side and is as isolated as possible by using a high vacuum, low thermally conductive wiring, and mounting. As a result, the mounted die connected to the hot and cold sides is subjected to a temperature gradient.

A thermal steady-state COMSOL simulation has been run to determine the optimal yet possible die size by sweeping different sizes and comparing them to choose the ideal die and PCB size. By simulating an auto-scaling 3-dimensional model of the PCB with a GaN Die and heater, different die sizes can be simulated to find the temperature difference over the die. An example model used for the sweeping die-sizes is shown in Figure 4.2. In this model, an overlapping space of 5 mm is used on each side to glue the die to the PCB for an ideal thermal connection between the two.

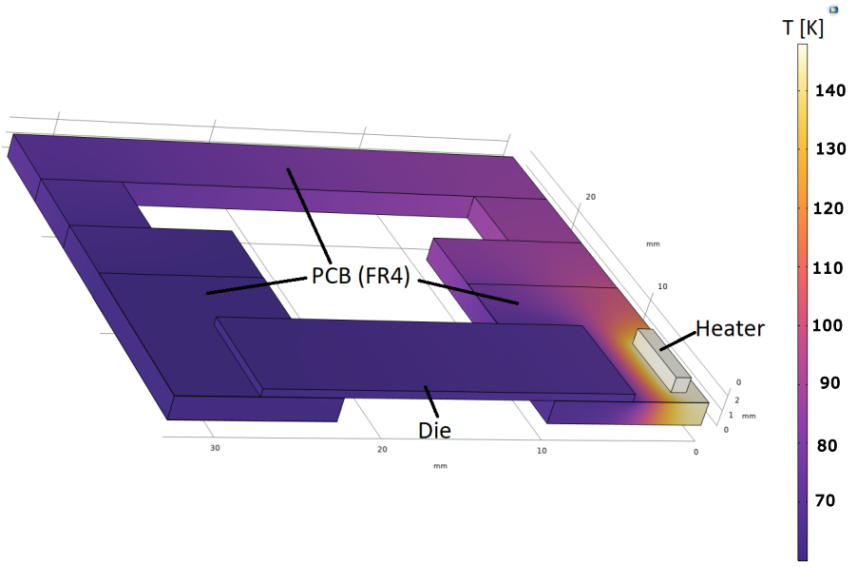


Figure 4.2: A 3-Dimensional COMSOL model used to determine the temperature difference over the GaN die with a 2 Watt heater

By varying the GaN die width and length, an optimum between length, width and temperature difference can be found. The optimum is defined by the overall resistance of the complete die and thermal conductivity of the die, both controlled by the width and length. As a result, for low resistance a wide and short die is ideal at the cost of thermal conductance, resulting in a lower temperature difference. Therefore, an ideal compromise must be found during a set of COMSOL simulations. During these simulations, the built in heat-conductivity of Si was used for the die since the die is mostly made out of Si. The heat conductivity of the FR4 PCB was gathered from Woodcraft et al. [34], where the thermal conductivity of $0.0001 - 1W/mK$ was measured over a temperature range of 0.1 - 400 Kelvin. Figure 4.3 shows the resulting temperature difference with different widths and lengths. Where the temperature difference over the die is plotted on the y-axis and the length of the die on the x-axis, each line represents a different die width, as denoted as W_s in the legend.

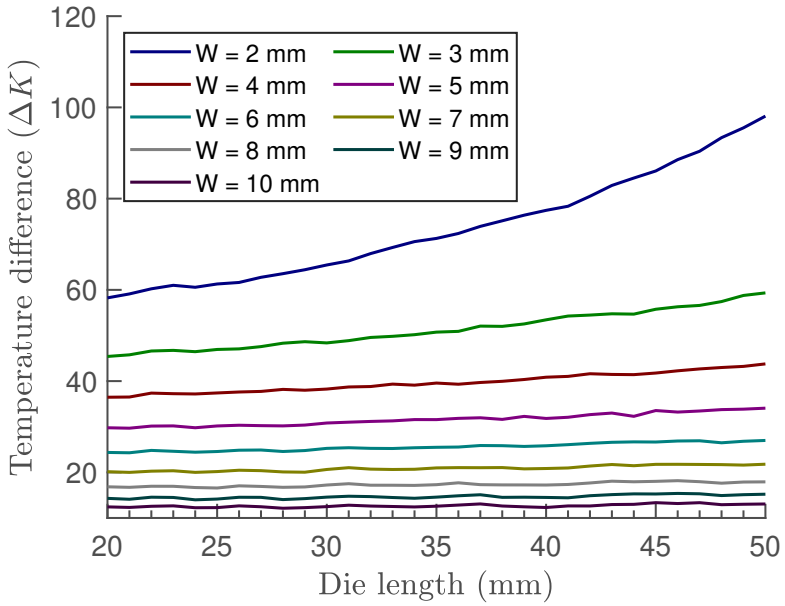


Figure 4.3: COMSOL simulation result of temperature difference over die, where different die widths (W) and lengths are compared

As a result, a 5 mm wide and 25 mm long die has been chosen as the ideal geometry. Using 5 mm wide dies allows the re-dicing of 25 by 25 mm dies into five individual dies, simplifying the fabrication process. A render of the designed PCB can be seen in Figure 4.4, where both the mounting area for the die and the earlier mentioned DT670 temperature sensors can be seen.

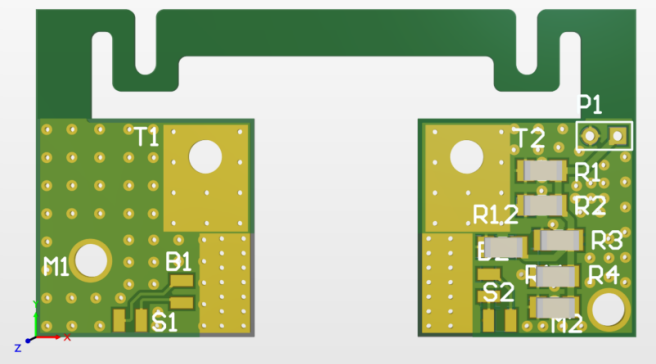


Figure 4.4: Model of designed PCB to create temperature gradient over the die, showing heating resistors on the right, two temperature sensor mounting pads T1 and T2, and a die mounting area with two bonding pads

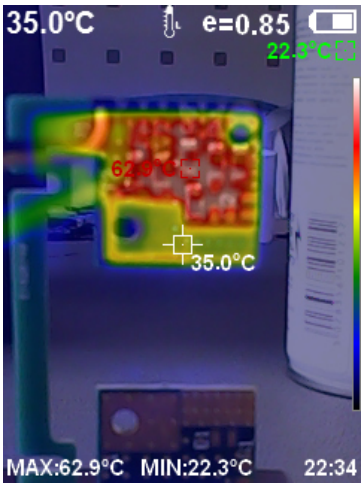


Figure 4.5: Thermal imaging of PCB with 1 Watt heating after 5 minutes, showing uniformity on the die and temperature sensor mounting pads

An initial room-temperature, non-vacuum heating test has been carried out to confirm the COMSOL simulation and determine the overall heat spread of the heater on the hot side of the PCB. As seen in Figure 4.5, a temperature difference between the hot and cold sides of 15 degrees Kelvin is reached. Ideally, no temperature difference between the temperature sensor and die mounting area is present to give a correct reading. From this thermal image, it can be noted that the temperature difference is negligible.

The same PCB is used without the copper block and heating resistors for the four-point measurements. As a result, the complete PCB contacts the cooler surface, cooling down the whole DUT. Four bonding pads are present on the PCB to contact all four points on the die to conduct measurements properly.

4.2. GaN on Silicon

Due to the absence of equipment at the TU Delft to epitaxially grow GaN on Silicon substrate , a custom wafer was specified for growth at a commercial company. As a result, it was only possible to order one wafer due to the high costs of the processes carried out to make said structures. Using a singular wafer also limited the earlier-mentioned goal of mapping the sheet hole density and PF since only one data point is now available.

Therefore, a new goal was set to prove the presence of a 2DHG within the chosen structure, measuring the conductivity, Seebeck coefficient, and thus its PF over a temperature range. These measurements can then be compared with the proposed simulation models to determine the accuracy of the simulation method. Alongside the simulation comparison, these measurements can be used to determine the need for further research in the feasibility for GaN based TEGs.

To mitigate the risk of surface cracking due to strain induced by the AlGaN polarizing layer, the thickness of the AlGaN layer was minimized. As a result, a structure with a lower hole sheet density was chosen than was anticipated earlier. The resulting structure is described in Table 4.1.

Layer	Material	Thickness	Other
1 (Surface)	p-GaN	30 nm	Mg doped, 3E19
2	u-GaN	20 nm	–
3	$Al_xGa_{1-x}N$	50 nm	x = 0.2
4	u-GaN	1 um	–
5	Buffer	2.4 um	–
6 (Bottom substrate)	Si	625 um	P-type, resistivity $< 0.03\Omega \cdot cm$

Table 4.1: Structure of ordered GaN on Si wafer for experimental measurements

As seen in the overview of the used structure, the p-GaN layer discussed and chosen in subsection 3.5.1 has been fabricated as intended. Whereas a 20 nm unintentionally doped GaN is used for the 2DHG to form in, also as intended. The AlGaN layer has been reduced in thickness to minimize the risk of cracks while still reliably forming a 2DHG according to the earlier performed simulations in subsection 3.5.2. With an aluminum content (x) of 20 %, a hole density of $5 \cdot 10^{12} cm^{-2}$ is expected. The AlGaN is placed on top of another unintentionally doped GaN in which an electron gas can form. The substrate used in this work is a 625 um thick Silicon layer, with a <111> rotation to minimize the lattice mismatch with the GaN layer (layer 4). In between the bottom substrate and u-GaN, a buffer layer is added to overcome the inevitable lattice mismatch between the u-GaN and <111> Silicon substrate.

This structure shows the compatibility of GaN on Si for future works using GaN in TEGs, since Si can be used for more intricate circuits and is easier to manipulate for further improvements. Examples of such enhancements include the back-etching of the Si to limit heat transport.

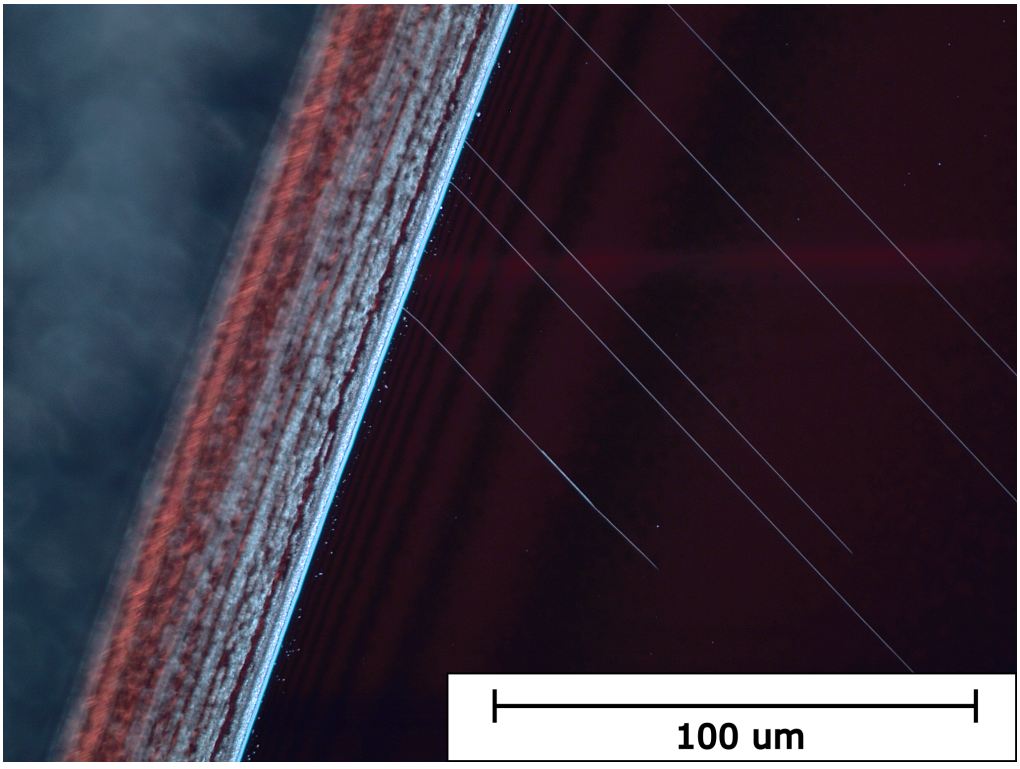


Figure 4.6: Surface cracking found at wafer edges due to non-uniform depositions

After inspection of the ordered wafers, several cracks can be observed at the wafer edges. An image of the cracks on the edge of the wafers is shown in Figure 4.6. The wafer cracking is formed due to the non-uniformity of the MOCVD process used during the GaN and AlGaN process. An edge exclusion zone of 5 mm is therefore taken into account during dicing of the wafer.

4.3. Ohmic contacts

To extract power from a TEG and properly measure its characteristics, a proper electrical connection to the 2DHG is required. Huy-Binh Do et al. [11] have investigated the origins of a Schottky barrier to a 2DHG in an Gold (Au)/Nickel (Ni)/GaN/AlGaN/GaN double heterostructure, in which the use of a Ni/Au metal contact is investigated.

4.3.1. Ni/Au contact to p-GaN

Due to its wide band gap of 3.4 eV, the p-type GaN has a high work function, resulting in limited methods to contact the p-GaN electrically. A select list of metals can contact the p-GaN to overcome the high work function. Ni, with its 5.5 eV work function and outstanding adhesion properties, therefore, is a viable solution. A Au capping layer is deposited on top of the Ni to further improve the metal contacts in terms of compatibility.

Despite the high metal work function of Ni, a Schottky-barrier still forms, with a barrier of 0.2 - 0.27 eV. To overcome this barrier, the Ni/Au metals must be annealed. This annealing process is commonly used for contacting the p-GaN layer, as done by Chen L. et al. [9], Jin-Kuo Ho et al. [16] to further improve the resistivity and overcome Schottky behavior.

Various Ni and Au thicknesses have been used in state-of-the-art research, where the annealing temperature and environmental gasses have been tested to find the optimal process [22, 17, 9, 26]. Multiple state-of-the-art results conclude the use of an oxygen-rich environment, a similar air-mixture as available to us in ambient air. Furthermore, an annealing temperature of 550 degrees Celsius is recommended for optimal results.

With careful consideration, a 20/100 nm Ni/Au metal contact was tested in this work, where an annealing temperature of 550 degrees Celsius at 10 minutes in ambient air was used. An ambient environment enables oxygen atoms to bind to the Ni layer through oxidation, forming an intermediate Nickel Oxide layer, which acts as a highly doped p-type layer. This NiO layer prevents the formation of a Schottky barrier, creating an ohmic metal to p-GaN as a result as desired.

4.3.2. Tunneling behaviour through p-GaN/u-GaN to 2DHG

The now contactable p-GaN through the Ni/Au metal contacts, can contact the formed 2DHG by hole tunneling through the p-GaN and u-GaN, as illustrated in Figure 4.7. This method has been proposed by Huy-Binh Do, et al. [11], where a contact resistivity of $5.3 \cdot 10^{-4} \Omega cm^2$ is achieved with a non-ideality factor of 6. The performance of the metal contacts is measured and discussed in subsection 5.2.1.

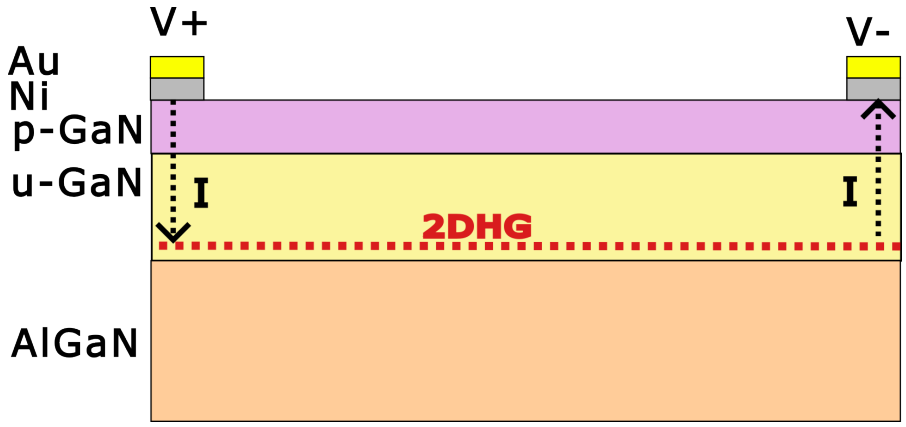


Figure 4.7: Tunneling to 2DHG through the p-GaN and u-GaN layers

4.3.3. Titanium Gold bonding contacts

As a result of the annealing process for the Ni/Au metal contacts and their low thickness, contacting the metal contacts directly risks damaging the Ni/Au contacts. Therefore, an extra metal deposition must be considered to enable ball-bonding pads on top of the Ni/Au metal contacts. A thin 10 nm Titanium layer is evaporated on top of the annealed Ni/Au metal layers as an adhesion layer, where a thicker 200 nm Gold layer is evaporated on top of the Titanium (Ti) as a top layer to enable bonding to test pads of measurement PCBs.

4.4. Metal contact fabrication and results

To realize the metal contacts on the GaN surface a short overview of the significant steps taken is provided below.

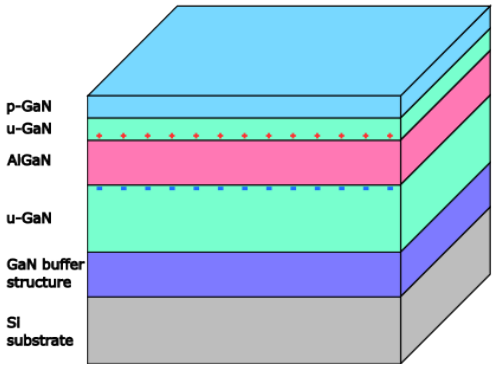


Figure 4.8: Illustration of clean GaN on Si Die

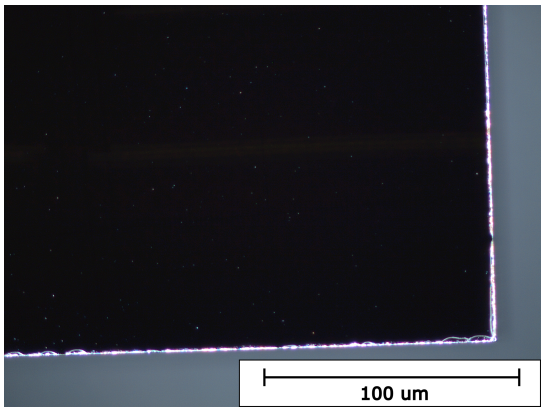


Figure 4.9: Microscope image of diced corner after DMSO cleaning

Firstly, the GaN wafer is diced into 25 by 25 mm dies to minimize the risk of breaking the whole wafer in the process and making different structures per die possible, a complete dicing map of the 4-inch wafer can be found in Appendix C. During dicing, a thick photoresist layer is spun onto the wafer to prevent damage and debris from the dicing process. After dicing, the individual dies are then cleaned for organic residue using Dimethylsulfoxide (DMSO) before surface passivation with Ammonium hydroxide (NH4OH), leaving a clean square die as illustrated in Figure 4.8. Figure 4.9 shows a microscope image of a die corner after dicing and cleaning with DMSO, showing clean dicing lines with little to no debris. Furthermore, no surface cracks are observed. This inspection is carried out for all 25x25 dies, to determine the usability of each die and ensure no unexpected problems are present later on in the fabrication or measurements.

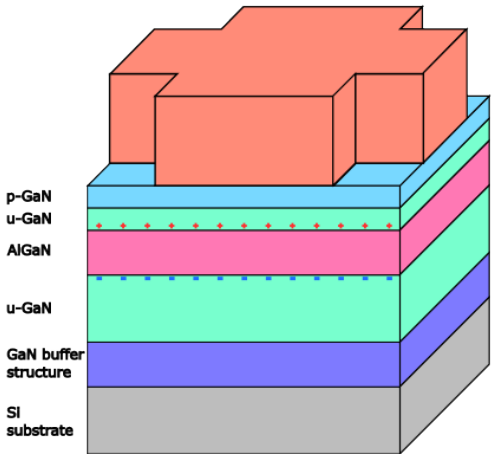


Figure 4.10: Illustration of shadow mask on die

A tape-like shadow mask is applied to the surface after NH4OH cleaning to select where a metal is deposited, illustrated in Figure 4.10. A Kapton tape sheet has been cut in the desired patterns using

a plotter-cutter with a resolution of 0.5 mm. The resolution of the plotter-cutter limits the size of the structures deposited significantly. However, the metal contact pads to contact the 2DHG do not require higher resolutions since the pad sizes have been chosen to be several millimeters long and wide.

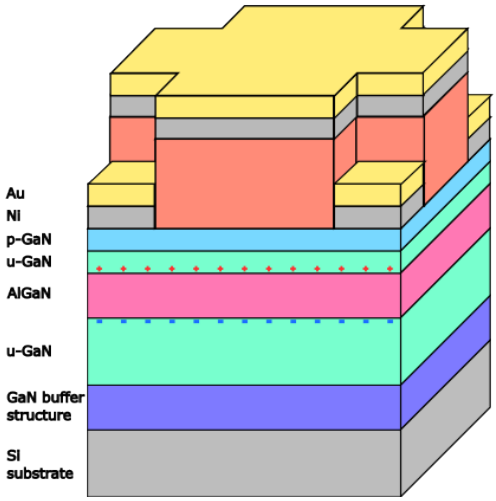


Figure 4.11: Illustration of evaporated metals on top of die with mask

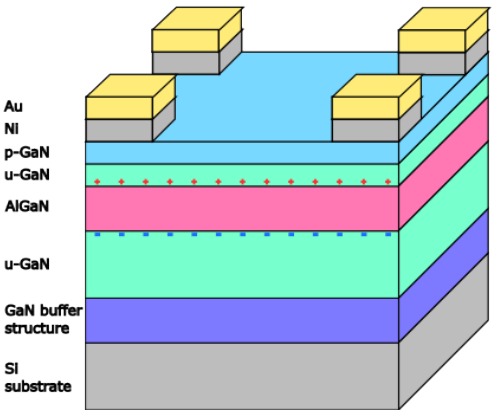


Figure 4.12: Illustration of evaporated metals after removing mask

A 20 nm thick Ni and 100 nm thick Au is then deposited through evaporation without breaking the vacuum, as illustrated in Figure 4.11. After evaporation, the shadow mask, including its residues, is removed, leaving only the metals where no mask was present, as illustrated in Figure 4.12.

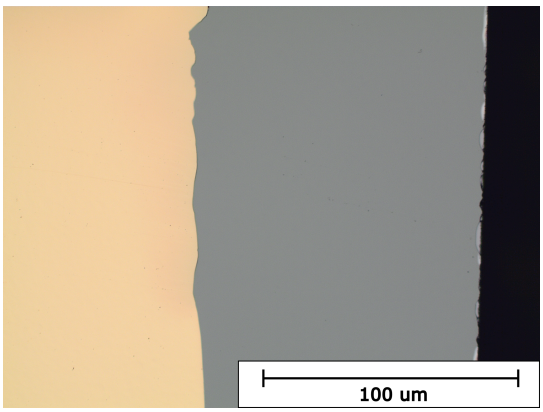


Figure 4.13: Microscope image of Ni/Au deposited on GaN surface, showing in-ideality of using a Kapton-tape mask and making sure the metal contact does not overlap the die edges

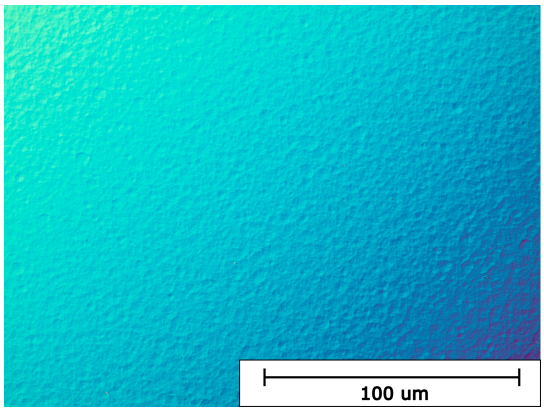


Figure 4.14: Microscope image of Ni/Au deposition through polarizing filter to determine the deposition quality

Figure 4.13 shows a microscope image of the deposited Ni/Au on the GaN surface. This image clearly shows non-straight lines caused by the Kapton tape used as a shadow mask. This image is mostly used to determine how close the Ni/Au metal is deposited to the wafer edges. No metal must be deposited onto the die edges, as it risks contacting the Si substrate, as it will interfere with measurement results.

Furthermore, Figure 4.14 shows a microscope image using a polarization effect to visualize the uniformity of the deposited layers. This image indicates a good uniform layer has been deposited during the metal evaporation phase of the die fabrication. This inspection is done for all the dies to identify in-ideality that results in risks during measurements.

The resulting die is annealed using a preheated oven at 550 degrees Celsius to create ohmic contacts, with ambient air as the environment. A similar shadow mask is applied to repeat the evaporation process for a 10 nm Ti and 200 nm Au metal layer on top of the already present Ni/Au metals, as illustrated in Figure 4.15. The die with deposited metal stack can then be diced into smaller pieces if necessary and mounted onto a PCB, which can be bonded for external electrical connections in the measurements setup.

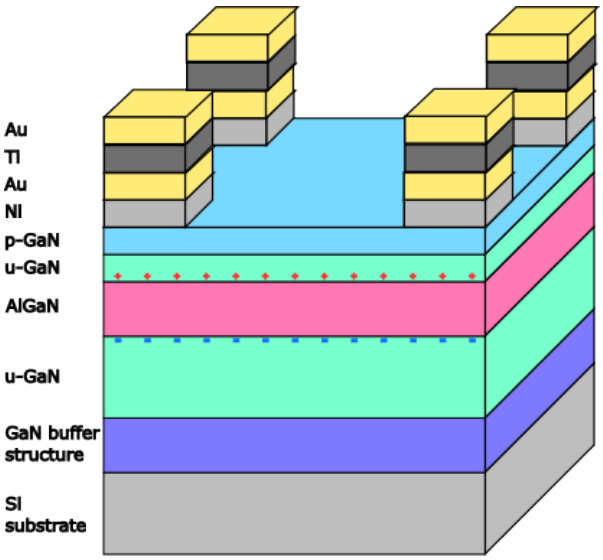


Figure 4.15: Illustration of resulting die with Ni/Au/Ti/Au metal stacks

The smaller dies are then glued to the PCB, with non-outgassing epoxy resin that is thermally conductive yet not electrically conductive. The thermally conductive glue is necessary to bond the die to the hot and cold sides of the PCB to reliably apply a thermal difference over the die in the Seebeck coefficient measurements. Furthermore, the die substrate is electrically isolated from the PCB to minimize accidentally applying a voltage between the top and bottom of the structure. A picture of the completed setup for the Seebeck coefficient measurements can be seen in Figure 4.16, in which the earlier illustrated setup in Figure 4.1 is realized and mounted, including glued die with fabricated metal contacts that are bonded to the PCB and temperature sensors on both sides of the die.

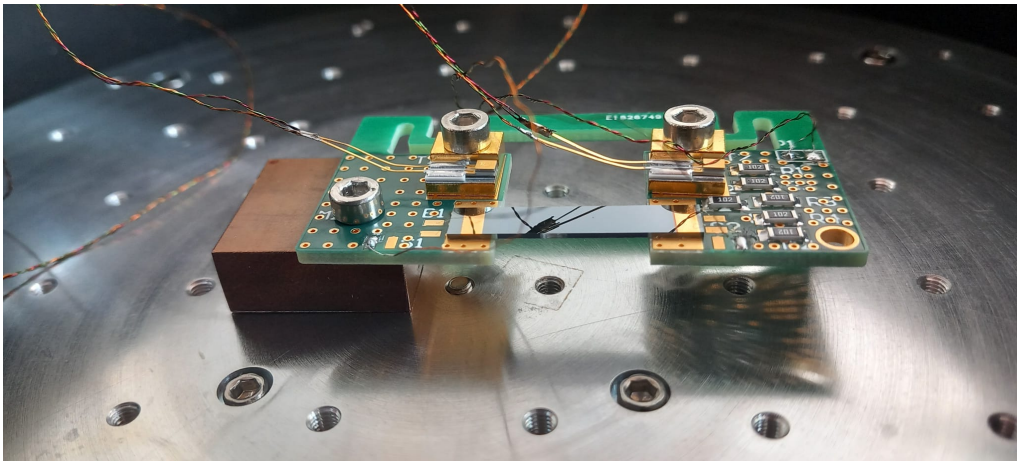


Figure 4.16: Picture of mounted DUT, with fabricated die with metal contacts bonded and glued to the designed PCB. Including soldered cryogenic wiring, temperature sensors and resistance heating elements

5

2DHG measurement results and discussion

The fabricated and prepared dies are thoroughly measured to determine their performance. This chapter thoroughly discusses the measurement setups used to characterize the GaN based 2DHG and shows and discusses the measurement results of the fabricated dies. The chapter then concludes with multiple discussions about the measurement results.

5.1. Measurement setups

Multiple measurements have characterized and determined the performance of the 2DHG. During these measurements, two different setups were used:

- A probe station for room-temperature I-V measurements
- A vacuum chamber with a cryogenic cooler for cryogenic temperature sweeps.

A simple probe station with four movable probes contacts the metal contacts on the GaN on Si die to perform 4-pt I-V measurements. A voltage sweep is performed using a Yokogawa GS210 Source Measure Unit (SMU), of which the results can be found in subsection 5.2.1.

The cryogenic cooler setup is used to take two different measurements to determine the Seebeck coefficient and sheet resistance over a range of various measurements. Both measurements use the cryogenic measurement setup similarly, of which an overview is provided in Figure 5.1.

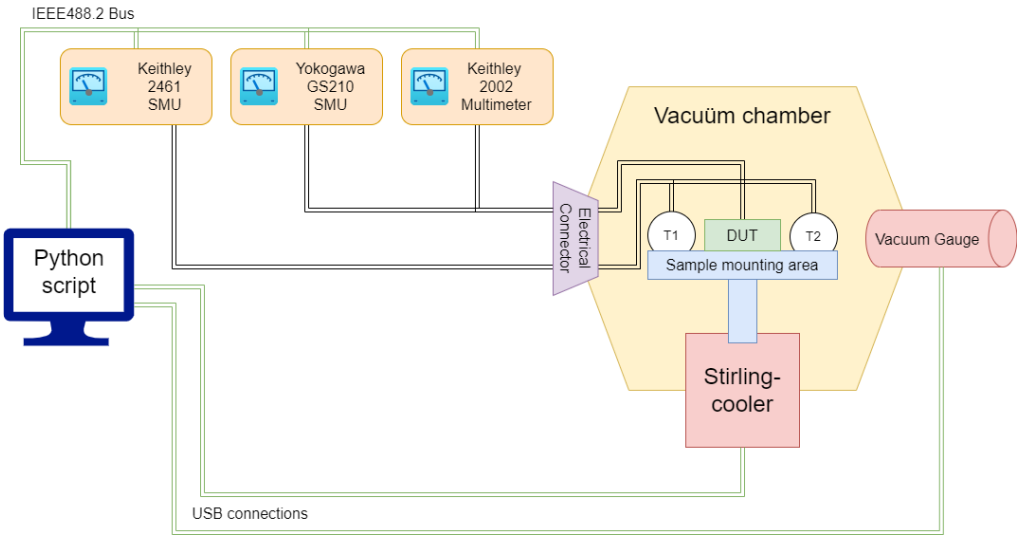


Figure 5.1: Overview of the cryogenic measurement setup, including measurement equipment and electrical connection diagrams

As can be seen in the figure, the DUT is placed inside a vacuum chamber, which can be seen in Figure 5.2. The vacuum chamber avoids the condensation of atmospheric nitrogen, oxygen, and other gases. A high vacuum also limits temperature fluctuations and heat transfer through convection, resulting in lower reachable temperatures and easier-to-reach temperature differences during the Seebeck coefficient measurements. A diaphragm and turbo-molecular pump reach vacuum levels in the 10^{-5} milli-bar range, which is boosted to a deeper vacuum when active cooling is turned on due to the ideal gas law.

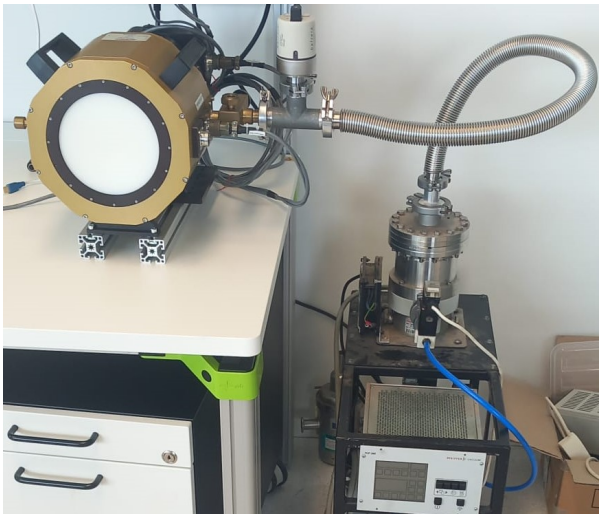


Figure 5.2: Photo of cryogenic cooler, including the vacuum chamber (left), pumps (right), and gauge (connected to hose)

The DUT is mounted on a designated metal mounting surface that is temperature-controlled with a Stirling cooler. This cooler can reach temperatures down to 50 Kelvin and is configurable using a USB connection with a general-purpose computer. The DUT is electrically connected through cryogenic cables that are electrically conductive but not thermally conductive to limit heat transport from the sample to the outer room temperature shell of the vacuum chamber. The measurement equipment devices connected to the DUT are a Yokogawa GS210 SMU and Keithley 2002 multimeter, dependent on the measurement carried out.

Two DT670 Silicon temperature sensor diodes from Lakeshore are available for temperature measurements on the DUT, marked as T1 and T2, with an accuracy of ± 1 Kelvin each. The temperature sensors are measured using a Keithley 2461 SMU by exciting them with $10\mu A$ and measuring their temperature-dependent voltage using a 4-wire measurement for minimal error.

A computer is connected to the measurement devices and Stirling-cooler. It can, therefore, control the measurement equipment and chamber temperature using different Python scripts to carry out long measurements. The cryo-cooler takes 10 hours to reach temperatures of 50 Kelvin from room temperature, making temperature sweeps long and susceptible to drift. As a result, substantial error margins are presented in the measurement result.

5.2. Measurement results

The following measurements were done to characterize the 2DHG:

- I-V contact resistance measurements at room-temperature (subsection 5.2.1)
- Four-point sheet resistance measurements with varying temperatures (subsection 5.2.2)
- Seebeck coefficient measurements with varying average die temperature (subsection 5.2.3)

The sheet resistance and Seebeck coefficient measurements are then combined to determine the Power Factor in subsection 5.2.4, where for all measurements, the relative error theory is applied as further elaborated in Appendix A

5.2.1. I-V characteristics metal contacts

With 4 wire current-voltage measurements, the metal contact to 2DHG electrical contact has been measured. By applying a range of differential Voltages onto the pads using the Yokogawa GS210, a function of the current is measured as seen in Figure 5.3. This measurement is carried out on the same die before and after annealing to determine the necessity of the annealing process. A completely linear response would be considered ideal, showing true Ohmic behavior.

As can be seen, little to no current was present at the applied voltages before annealing, whereas a more linear relation between the current and voltage can be seen within ± 2 V. This comparison shows the necessity and success of the proposed annealing process, required to form an ohmic reaction with the p-GaN top layer.

A clear linear response can be seen up to a range of ± 2 Volts, where above this voltage range the current starts to saturate. As mentioned in subsection 4.3.2, a form of tunneling was expected when contacting the 2DHG through the p-GaN and u-GaN layers between the metal contacts and 2DHG.

In conclusion, the annealing process is necessary to create ohmic behavior. Meanwhile, linear Ohmic behavior has been measured up to voltages of ± 2 Volts due to tunneling mechanisms through the p-GaN and u-GaN layers. During other measurements, the maximum range of 2 Volts must be followed to stay within the ohmic range of the metal contacts.

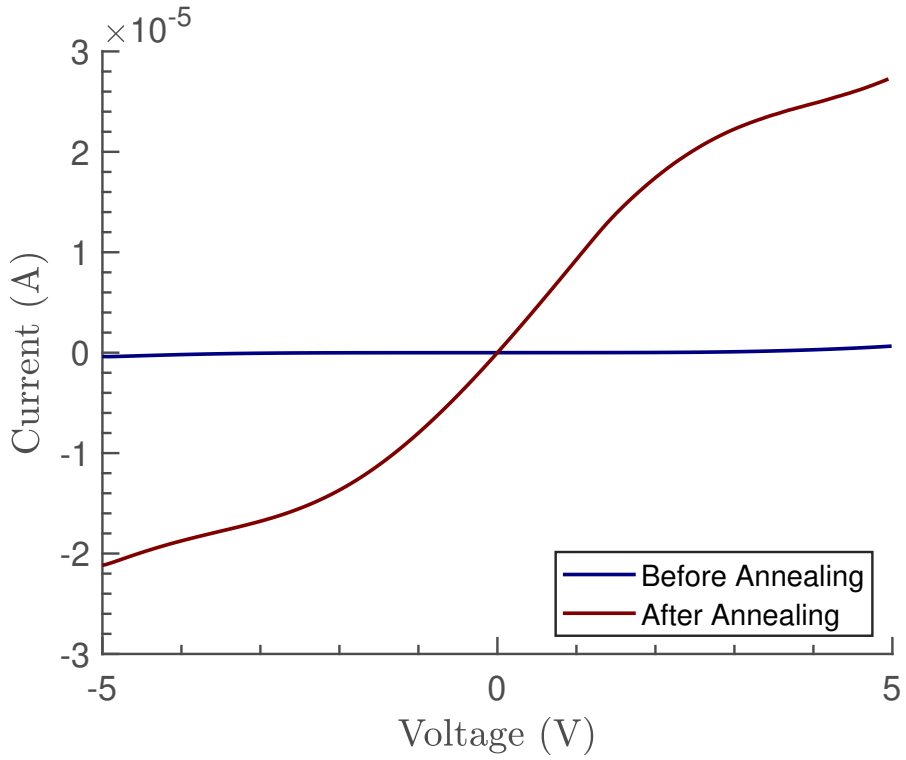


Figure 5.3: Current Voltage response curves of metal contact to 2DHG

5.2.2. Four-point sheet resistance measurements

A four-point measurement has been carried out on a 25 by 5 mm die, on which 4 pads have been deposited as explained in section 4.3. An illustration of the 4-point sheet resistance measurement can be seen in Figure 5.4. A current of $10\mu A$ is applied between I- and I+ using a Yokogawa GS21s and a Voltage measurement is carried out on the V+ and V- pads using a Keithley 2002 multimeter. The sheet-resistance can be determined using Equation 5.1 where w and l represent the width and length of the distance between the inner pads. This measurement is carried out in the cryo-cooler setup to sweep the die temperature from 50 to 300 Kelvin, and is plotted in Figure 5.5.

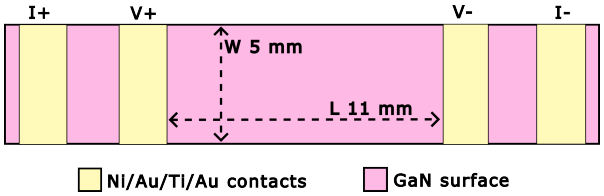


Figure 5.4: Illustration of 4-pt measurement metal contacts on GaN on Si die

$$R_{sh} = \frac{V_2 - V_1}{I_2 - I_1}\frac{w}{l} \tag{5.1}$$

As can be seen, the simulated sheet resistance of the structure used during fabrication is added to compare the results. Comparing the measured and simulated sheet resistance of the GaN structure shows a 7 times higher measured sheet resistance than the simulated result. As mentioned in section 3.2, the simulated conductivity was significantly higher than state-of-the-art measurements. A similar order of magnitude difference is shown here, confirming mismatching simulation results compared to realized measurements.

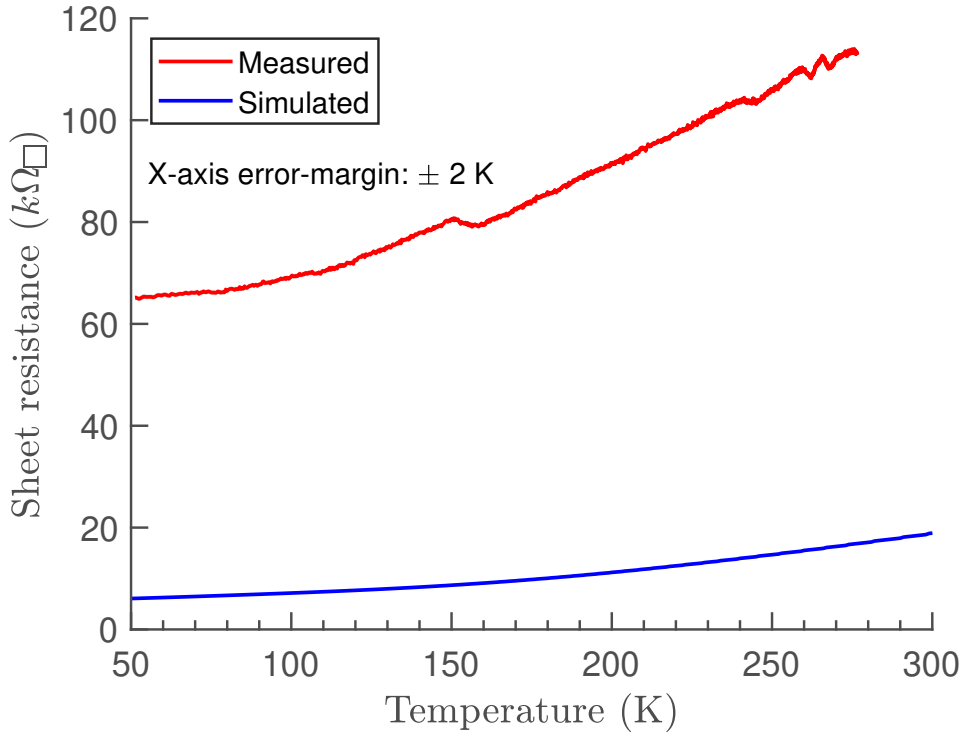


Figure 5.5: Sheet resistance measurement over temperature, compared with simulation

Upon further inspection, it can be noted that the sheet resistance trend over temperature is accurate if the magnitude difference is disregarded. Concluding that the scattering mechanisms and sheet

density considered in the simulations mostly mismatch in magnitude. Upon further investigation, different reasons can affect this discrepancy, such as the un-intentional Si dopants lowering the sheet hole density or incorrectly assumed constants during the simulation process, such as the dislocation factor and surface roughness, both affecting different scattering mechanisms.

A point of interest in the measurements can be noted around the 150 Kevlin region, where a local maximum can be found that is not shown in the simulation data. This local maximum found in the simulation is most likely due to unknown setup issues but requires further investigation.

In conclusion, the sheet resistance increases with temperature as expected, whereas the simulated magnitude of the sheet resistance is off by a factor of 7. To further investigate the reason behind said discrepancies, it is therefore recommended to measure the hall-mobility and sheet hole density individually to identify the reason behind this mismatch with the simulation results.

5.2.3. Seebeck coefficient measurements

By loading the designed PCB, including the diving board principle and on PCB heater as explained in section 4.1 the Seebeck coefficient is measured. By cooling down the chamber, one side of the PCB is being actively cooled, whereas the hot side is equipped with resistive heaters to increase the temperature gradient over the mounted die. By then measuring the Voltage present on the GaN die using the fabricated metal contacts, using a Keithley 2002 multimeter, the Seebeck Voltage (V_s) can be extracted. The earlier introduced temperature sensors are mounted on the hot and cold side, represented as T1 (cold) and T2 (hot) in Equation 5.2, where $V_1 - V_2$ represents the measured voltage over the die (with V_1 representing the hot side and V_2 the cold side).

$$S = -\frac{V_2 - V_1}{T_2 - T_1} \tag{5.2}$$

Figure 5.6 shows the Seebeck coefficient over the average die temperature, which is calculated using Equation 5.3. In order to minimize measurement errors due to temperature sensor inaccuracy, the temperature difference was maximized. A minimum average temperature without significant measurement errors reached 100 Kelvin, resulting in measurement results between 100 Kelvin and 300 Kelvin.

$$T_{avg} = \frac{T_1 + T_2}{2} \tag{5.3}$$

Firstly, the polarity of the Seebeck coefficient was expected to be positive, which was confirmed using measurements. Furthermore, the Seebeck effect in a 2DHG is confirmed using these measurements while showing an increase in the Seebeck coefficient over temperature.

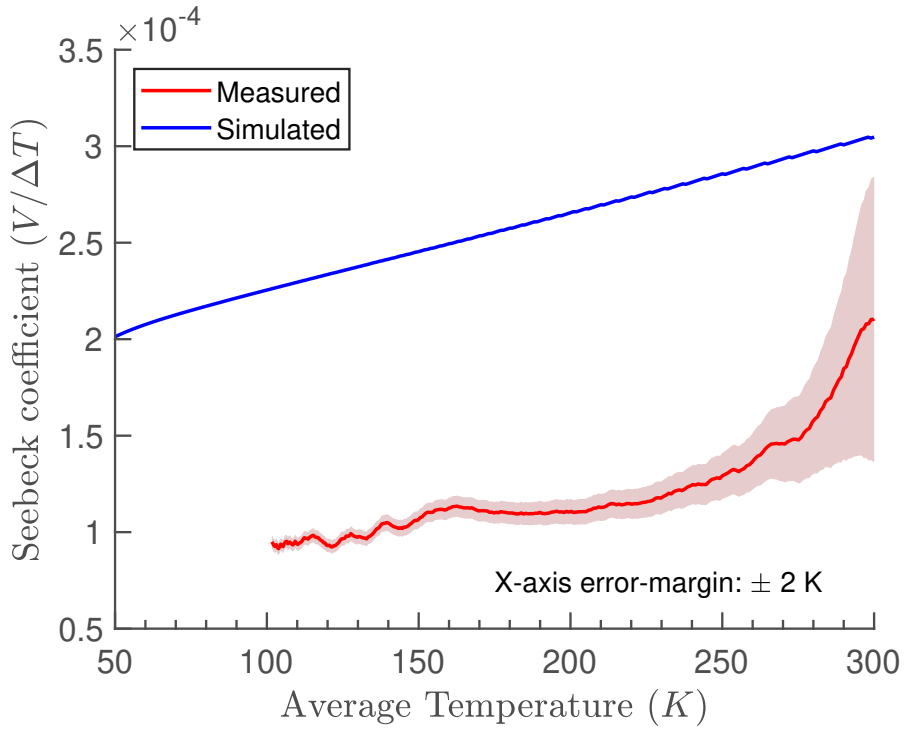


Figure 5.6: Seebeck-coefficient measurement over temperature, compared with simulation

A lower Seebeck coefficient was measured than was simulated earlier. Furthermore, a steep increase in the Seebeck coefficient measurements is seen at higher temperatures. The simulation results show a steady linear increase in the Seebeck coefficient, where the measured increase of the Seebeck coefficient is minimal in the lower temperature range and increases significantly for higher temperatures. The measurement error, however, increases considerably over temperature as well due to the lower temperature difference reached at higher temperatures. As a result, it can be stated that the steep increase in the Seebeck coefficient can be caused by measurement inaccuracies. Therefore, a more reliable measurement setup is recommended to verify the steep increase of the Seebeck coefficient over temperature.

In conclusion, the performed measurement proves the Seebeck effect inside a 2DHG and confirms the order of magnitude of the Seebeck coefficient. A discrepancy is found between the simulated and measured change of the Seebeck coefficient with an increase in temperature. This is most likely caused by the measurement inaccuracies, it is therefore recommended to further investigate the Seebeck coefficient over temperature by using on-chip heaters and lock-in amplifier.

5.2.4. Power Factor

Finally, with the measured sheet resistance and Seebeck coefficient, the PF can be estimated. To do so, Equation 5.4 is used to determine the PF using the sheet resistance instead of the earlier seen conductivity.

$$PF = S^2 \frac{1}{R_s \cdot t} \tag{5.4}$$

As can be seen in Equation 5.4, the thickness (t) of the 2DHG is used to find the power density of the structure. According to the Nextnano simulations, a 2 nm thick 2DHG has formed.

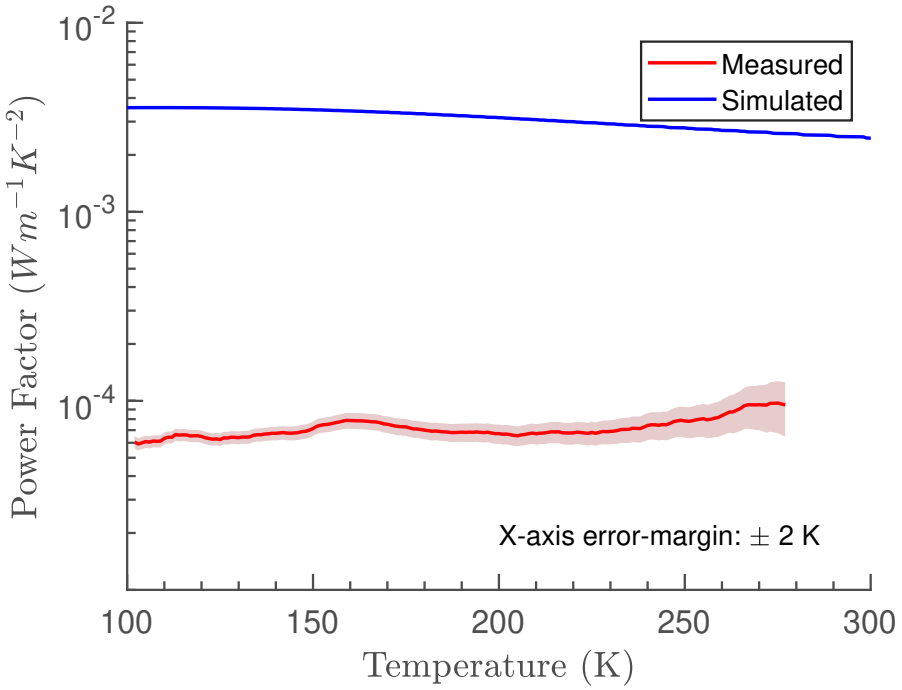


Figure 5.7: Experimentally determined Power factor over temperature, compared with simulation

With Equation 5.4, Figure 5.7 can be plotted over temperature. The earlier carried out simulations of the PF are also included to determine the accuracy of the simulations. This figure shows that the PF stays relatively constant over temperature, which can benefit wide temperature range use cases.

A clear difference in magnitude is seen by comparing the measured and simulated results. The difference between the measurement and simulation mostly relates to the earlier measured Seebeck coefficient and sheet resistance, discussed in subsection 5.2.3 and subsection 5.2.2.

In section 5.3, a deeper discussion about the overall performance of the 2DHG as a TEG is provided, discussing the problems by comparing the PF of a 2DHG with materials that do not rely on 2-Dimensional gasses.

5.3. Discussion

This section discusses the overall performance of the measured 2DHG performance by comparing it with other state-of-the-art materials. Firstly, a discussion about the method of comparing the power density of 2-dimensional gasses in general is given in subsection 5.3.1.

5.3.1. Power Factor of 2-Dimensional electron and hole gas based TEGs

When assessing different TEG materials, it is crucial to use metrics that allow for fair and meaningful comparisons. However, achieving this fairness becomes challenging when comparing 2-dimensional gases to doped bulk materials. In this work, the power factor (PF) is optimized and used as a comparative metric across different materials. However, the PF presents an unfair comparison when 2-dimensional gases are compared with bulk materials.

In the case of 2-dimensional gasses, the PF is determined exclusively within the quantum well (QW), which typically spans only 5-10 nm. This calculation disregards the complete structure necessary to form the QW, as seen in subsection 5.2.4. As a result, the full structure required to form a QW is not accurately represented when determining the PF of 2-dimensional gasses, leading to an uneven comparison with bulk materials that rely on dopant-based conduction.

In contrast to 2-dimensional gasses, doped bulk materials do not require a complete structure to form a conductive channel because of added dopants. As a result, the PF that can be calculated for bulk materials is much more representative of its material thickness and structure compared to 2-dimensional gasses.

A solution to overcome this unfair comparison is to integrate the minimal required structure thickness to form a QW as a percentage as shown in Equation 5.5, where the formed QW (t_{QW}) is divided by the minimally required structure thickness ($t_{struc.}$) to determine a sense of efficiency. This efficiency can then be incorporated in the PF directly to get the real power density of a QW based structure.

$$\%_{effectivethickness} = \frac{t_{QW}}{t_{struc.}} \tag{5.5}$$

A comparison with bulk materials clearly shows that bulk materials outperform QW-based TEGs, as the efficiency of most QW based TEGs is around 1 - 2 %, compared to bulk materials with 100 % efficiency.

Furthermore, selecting the total resistivity of a TEG leg by increasing the thickness of the conductive channel is considered an important optimization step in micro-TEG designs, as stated by Zhang et al.[38]. Changing the thickness of bulk-doped materials is relatively straightforward, as the thickness can be freely adjusted without significant impact. In structures that rely on QWs, the thickness of the QW is limited and cannot be increased. To be able to form a QW, careful considerations are required to create a conductive channel reliably, making 2-dimensional gas-based TEGs challenging to realize.

To increase the efficiency of QW based TEGs to compete with bulk materials, further methods are recommended to improve efficiency and provide easily controllable channel thicknesses. A method of increasing the efficiency and scalability of QWs in GaN could be the use of superlattices, in which a structure can be repeated to create a repeating pattern with multiple QWs. As a result, the amount of QWs can be freely chosen by selecting the amount of repeated structures to make N QWs. This results in a lower overall resistance in a similar structure that normally only contains one 2DEG and/or 2DHG structure. Sztein et al [33] has already proven that superlattices are able to improve GaN 2DEG based superlattices for thermoelectric properties.

5.3.2. GaN TEGs for extreme environments

In this work, GaN based TEGs have been investigated for their wide temperature range functionality. The 2DHG realized in this project, together with the earlier cited 2DEG of Yalamarthy et al. [29] shows that GaN based TEGs are a suitable solution as the PF stays constant over a temperature between 75 and 300 Kelvin. Compared to bulk materials that rely on doping, such as Bi_2Te_3 and Sb_2Te_3 (300 - 400 K), (375 K) or higher temperature TEG materials such as $PbTe$ (315 - 600), TiO_2 (425 - 650) [41, 18].

This work only investigated the extremely low-temperature range of GaN based 2DHG TEGs. It is known and proven that the temperature range of GaN 2DEGs can reach temperatures of up to 700 degrees Kelvin [20] . A similar high temperature, and thus also wide temperature range, is expected for but yet to be confirmed in GaN based 2DHGs.

6 Conclusion

This thesis investigated the use of GaN based TEGs by expanding upon the known performance of n-type 2DEG based TEG-characteristics. By introducing the formation of a 2DHG in a double hetero junction, a method to form a p-type GaN semiconductor has been introduced to further boost the performance of GaN based TEGs.

6.1. Main findings of this thesis

The formation of a 2DHG within the double-heterojunction has been proven with sheet-resistance measurement, proving that a 2DHG can be formed together with a 2DEG to further improve GaN TEGs. The formed 2DHG is then further characterized through simulations and measurements.

A sheet resistance of down to $70k\Omega_{\square}$ has been measured and compared with earlier performed simulations. A significant difference between the measured and simulated sheet resistance has been found, concluding that the mobility simulations require further polishing. A Seebeck Voltage on the 2DHG has been measured and simulated, proving that using a 2DHG as TEG is possible. A small error between the simulations and measurements is observed, which indicates that the newly proposed simulation method is reliable after some minor reconsideration. By measuring both the Seebeck voltage and temperature difference, a Seebeck Coefficient over a range of temperatures using a cryogenic cooler has been determined between $100\mu V$ and $200\mu V$. With both the Seebeck coefficient and sheet resistance, a constant power factor of $7 \cdot 10^{-4} W m^{-1} K_{-2}$ has been determined. The method in which the Power Factor is calculated for 2-dimensional Hole gasses is discussed, as it is not fairly comparable with other non-2-dimensional gasses.

In conclusion, the next step is taken for further investigation of GaN TEGs, where a p-type 2DHG has been tested. It has been proven that a 2DHG can be used to improve GaN TEG performance, although further investigation is necessary.

6.2. Outlook on future works

A 2DHG TEG was realized and characterized during this thesis. With the help of these findings, a set of recommendations for future works is given below:

Mobility measurements:
During this work, the conductivity of the 2DHG was determined using sheet resistance measurements. The sheet resistance of the 2DHG depends on the 2DHGs mobility and sheet hole density. Both individual metrics of the 2DHG should be examined in isolation to understand further the discrepancy between the simulated and measured sheet resistance. Separate comparisons of the measured and simulated sheet hole density and hall mobility would provide valuable general information for further research into 2DHG.

To measure the hole density and mobility individually, Hall mobility measurements and Van der Pauw measurements could provide the option to isolate both mechanisms for individual performance analysis. Therefore, it is recommended that mobility and hole density must be further investigated by

performing hall- and Vanderpauw-measurements.

Further measurements for power density over different sheet densities:
In the simulation phase of this work, the performance of 2DHG based TEGs is investigated over different sheet hole densities. The measurement results, however, were only based on one structure with a constant sheet hole density. As a result, the PF is only known for 2DHGs with a sheet hole density of $5 \cdot 10^{12} cm^{-2}$. To get a better understanding and optimize 2DHG based TEGs, it is therefore recommended to find the PF optimum over different sheet hole densities through measurements in addition to the already performed simulations.

GaN based TEG using 2DEG and 2DHG:
With this work's conclusion that a 2DHG can be used as a p-type TEG, and earlier research [29] showing the use of a 2DEG as n-type TEG. The next logical step would be the combination of both 2-dimensional gasses to boost the performance of GaN based TEGs. With the in this work investigated double hetero junction, a structure with a parallel 2DEG and 2DHG is formed. By interconnecting the 2DEG and 2DHG by etching away the mesa and depositing metals, electrical contacts can be made to attach both 2-dimensional gasses in series, as seen in Figure 6.1

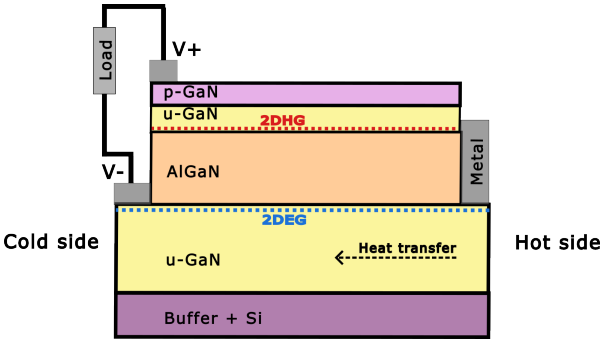


Figure 6.1: Proposed TEG structure utilizing 2DEG and 2DHG as n- and p-type

After further testing of the proposed design as shown, a device with a 2DHG and 2DEG as introduced above, more intricate structures can be investigated. Micro-TEG structures have been thoroughly researched to enable the use of double-heterostructures [38, 37].

Super-lattices to increase total Power Factor:
As discussed earlier in subsection 5.3.1, to increase the output power of GaN based TEGs, more efficient structures must be found to form a 2DEG or 2DHG. A proposed solution, used mostly in HEMT designs [33, 27], is the use of super-lattices, where multiple 2DHGs and 2DEGs can form in close vicinity. This can increase the power density of GaN greatly, making it an interesting topic for further improvements.

Overall conclusion:
In conclusion, the development of GaN based TEGs in its current state still requires significant research. This can be split into short-term and long-term work that expands upon this work. Further measurements of the mobility and sheet density of this work's structures to verify its performance are recommended. More long-term proposals to improve GaN based TEG performance are also given by combining a 2DHG with a 2DEG, and further investigation in the use of superlattices to increase the structure's efficiency effectively. This work has paved the way to apply the above-mentioned theories by proving the potential of a 2DHG in a double heterojunction for TEGs, making further research into improving TEGs possible.

References

[1] O Ambacher et al. “Role of Spontaneous and Piezoelectric Polarization Induced Effects in Group-III Nitride Based Heterostructures and Devices”. In: *physica status solidi (b)* 216.1 (1999), pp. 381–389. ISSN: 0370-1972. DOI: https://doi.org/10.1002/(SICI)1521-3951(199911)216:1<381::AID-PSSB381>3.0.CO;2-O. URL: https://doi.org/10.1002/(SICI)1521-3951(199911)216:1%3C381::AID-PSSB381%3E3.0.CO;2-O%20https://onlinelibrary.wiley.com/doi/10.1002/(SICI)1521-3951(199911)216:1%3C381::AID-PSSB381%3E3.0.CO;2-O.

[2] O Ambacher et al. “Two-dimensional electron gases induced by spontaneous and piezoelectric polarization charges in N- and Ga-face AlGaN/GaN heterostructures”. In: *Journal of Applied Physics* 85.6 (1999), pp. 3222–3233. ISSN: 0021-8979. DOI: 10.1063/1.369664. URL: https://doi.org/10.1063/1.369664.

[3] Samuel James Bader et al. “Prospects for Wide Bandgap and Ultrawide Bandgap CMOS Devices”. In: *IEEE Transactions on Electron Devices* 67.10 (Oct. 2020), pp. 4010–4020. ISSN: 15579646. DOI: 10.1109/TED.2020.3010471.

[4] Carsten Beckmann et al. “MOVPE-grown GaN/AlGaN heterostructures on sapphire with polarization-induced two-dimensional hole gases”. In: *Journal of Physics D: Applied Physics* 55.43 (Aug. 2022), p. 435102. ISSN: 0022-3727. DOI: 10.1088/1361-6463/AC89FF. URL: https://iopscience.iop.org/article/10.1088/1361-6463/ac89ff%20https://iopscience.iop.org/article/10.1088/1361-6463/ac89ff/meta.

[5] Thomas E. Beechem et al. “Size Dictated Thermal Conductivity of GaN.” In: *Journal of Applied Physics* 120.9 (Apr. 2017). ISSN: 0021-8979. DOI: 10.1063/1.4962010.

[6] Stefan Birner et al. “nextnano: General Purpose 3-D Simulations”. In: *IEEE Transactions on Electron Devices* 54.9 (2007), pp. 2137–2142. DOI: 10.1109/TED.2007.902871.

[7] C Bryan et al. “Thermoelectric Properties of n-type GaN and 2D Electron Gas in AlGaN-GaN Heterostructure”. In: *Journal of Electronic Materials* 50.3 (2021), pp. 1301–1306. ISSN: 0361-5235. DOI: 10.1007/s11664-020-08652-3. URL: https://dx.doi.org/10.1007/s11664-020-08652-3.

[8] Reet Chaudhuri et al. “A polarization-induced 2D hole gas in undoped gallium nitride quantum wells.” In: *Science (New York, N.Y.)* 365.6460 (Sept. 2019), pp. 1454–1457. ISSN: 0036-8075. DOI: 10.1126/science.aau8623.

[9] Li-Chien Chen et al. “Microstructural investigation of oxidized Ni/Au ohmic contact to p -type GaN”. In: *Journal of Applied Physics* 86.7 (Oct. 1999), pp. 3826–3832. ISSN: 0021-8979. DOI: 10.1063/1.371294. URL: https://pubs.aip.org/jap/article/86/7/3826/688204/Microstructural-investigation-of-oxidized-Ni-Au.

[10] Kevin J. Chen et al. “GaN-on-Si power technology: Devices and applications”. In: *IEEE Transactions on Electron Devices* 64.3 (Mar. 2017), pp. 779–795. ISSN: 00189383. DOI: 10.1109/TED.2017.2657579.

[11] Huy Binh Do, Jinggui Zhou, and Maria Merlyne De Souza. “Origins of the Schottky Barrier to a 2DHG in a Au/Ni/GaN/AlGaN/GaN Heterostructure”. In: *ACS Applied Electronic Materials* 4.10 (Oct. 2022), pp. 4808–4813. ISSN: 26376113. DOI: 10.1021/ACSAELM.2C01138/ASSET/IMAGES/LARGE/EL2C01138{_}0004.JPEG. URL: https://pubs.acs.org/doi/full/10.1021/acsaelm.2c01138.

[12] Gang Chen. *Nanoscale Energy Transport and Conversion, A parallel treatment of electrons, molecules, phonons and photons*. Massechusetts: Massachusetts Institute of Technology, 2005. ISBN: 978-0195159424.

[13] M N Gurusinghe, S K Davidsson, and T G Andersson. “Two-dimensional electron mobility limitation mechanisms in Al x Ga 1−x N / GaN heterostructures”. In: (). DOI: 10.1103/PhysRevB.72.045316.

[14] Ahmad Hassan, Yvon Savaria, and Mohamad Sawan. “GaN Integration Technology, an Ideal Candidate for High-Temperature Applications: A Review”. In: *IEEE Access* 6 (2018), pp. 78790–78802. ISSN: 21693536. DOI: 10.1109/ACCESS.2018.2885285.

[15] Kazuhiko Hirakawa and Hiroyuki Sakaki. “Mobility of the two-dimensional electron gas at selectively doped n-type Al Gai ”As/GaAs heterojunctions with controlled electron concentrations”. In: 33 (1986).

[16] Jin Kuo Ho et al. “Low-resistance ohmic contacts to p-type GaN”. In: *Applied Physics Letters* 74.9 (Mar. 1999), pp. 1275–1277. ISSN: 0003-6951. DOI: 10.1063/1.123546. URL: /aip/apl/article/74/9/1275/107881/Low-resistance-ohmic-contacts-to-p-type-GaN.

[17] Jin-Kuo Ho et al. “Low-resistance ohmic contacts to p-type GaN achieved by the oxidation of Ni/Au films”. In: (1999). URL: http://jap.aip.org/jap/copyright.jsp.

[18] Nesrine Jaziri et al. “A comprehensive review of Thermoelectric Generators: Technologies and common applications”. In: *Energy Reports* 6 (Dec. 2020), pp. 264–287. ISSN: 2352-4847. DOI: 10.1016/J.EGYR.2019.12.011.

[19] Ashutosh Kumar et al. “Growth of p-type GaN – The role of oxygen in activation of Mg-doping”. In: *Power Electronic Devices and Components* 5 (June 2023), p. 100036. ISSN: 2772-3704. DOI: 10.1016/J.PEDC.2023.100036.

[20] Narihiko Maeda et al. “High-temperature electron transport properties in AlGaN/GaN heterostructures”. In: *Applied Physics Letters* 79.11 (Sept. 2001), pp. 1634–1636. ISSN: 0003-6951. DOI: 10.1063/1.1400779. URL: /aip/apl/article/79/11/1634/514362/High-temperature-electron-transport-properties-in.

[21] Alan J.H. McGaughey et al. “Size-dependent model for thin film and nanowire thermal conductivity”. In: *Applied Physics Letters* 99.13 (Sept. 2011), p. 33. ISSN: 00036951. DOI: 10.1063/1.3644163/340780. URL: /aip/apl/article/99/13/131904/340780/Size-dependent-model-for-thin-film-and-nanowire.

[22] D. Mistele et al. “Investigation of Ni/Au-contacts on p-GaN annealed in different atmospheres”. In: *Journal of Crystal Growth* 230.3-4 (Sept. 2001), pp. 564–568. ISSN: 0022-0248. DOI: 10.1016/S0022-0248(01)01250-7.

[23] Akira Nakajima et al. “Generation and transportation mechanisms for two-dimensional hole gases in GaN/AlGaN/GaN double heterostructures”. In: *Journal of Applied Physics* 115.15 (Apr. 2014), p. 153707. ISSN: 10897550. DOI: 10.1063/1.4872242/138918. URL: /aip/jap/article/115/15/153707/138918/Generation-and-transportation-mechanisms-for-two.

[24] Akira Nakajima et al. “High density two-dimensional hole gas induced by negative polarization at GaN/AlGaN heterointerface”. In: *Applied Physics Express* 3.12 (Dec. 2010), p. 121004. ISSN: 18820778. DOI: 10.1143/APEX.3.121004/XML. URL: https://iopscience-iop-org.tudelft.idm.oclc.org/article/10.1143/APEX.3.121004%20https://iopscience-iop-org.tudelft.idm.oclc.org/article/10.1143/APEX.3.121004/meta.

[25] Akira Nakajima et al. “Temperature-independent two-dimensional hole gas confined at GaN/AlGaN heterointerface”. In: *Applied Physics Express* 6.9 (Sept. 2013), p. 091002. ISSN: 18820778. DOI: 10.7567/APEX.6.091002/XML. URL: https://iopscience-iop-org.tudelft.idm.oclc.org/article/10.7567/APEX.6.091002%20https://iopscience-iop-org.tudelft.idm.oclc.org/article/10.7567/APEX.6.091002/meta.

[26] D Qiao et al. “A study of the Au/Ni ohmic contact on p-GaN”. In: *Journal of Applied Physics* 88.7 (Oct. 2000), pp. 4196–4200. ISSN: 0021-8979. DOI: 10.1063/1.1311809. URL: /aip/jap/article/88/7/4196/291282/A-study-of-the-Au-Ni-ohmic-contact-on-p-GaN.

[27] Subhranshu Sekhar Sahu. “Thermoelectric enhancement of GaN/InxGa1−xN superlattice using interfacial polarization electric field”. In: *Materials Today Communications* 34 (Mar. 2023), p. 105073. ISSN: 2352-4928. DOI: 10.1016/J.MTCOMM.2022.105073.

[28] Ananth Saran Yalamarthy. “POLARIZATION FIELD ENHANCED TRANSPORT IN GALLIUM NITRIDE HETEROSTRUCTURES FOR ENERGY HARVESTING AND SENSING A DISSERTATION SUBMITTED TO THE DEPARTMENT OF MECHANICAL ENGINEERING AND THE COMMITTEE ON GRADUATE STUDIES OF STANFORD UNIVERSITY IN PARTIAL FULFILLMENT OF THE REQUIREMENTS FOR THE DEGREE OF DOCTOR OF PHILOSOPHY”. PhD thesis. 2019. URL: http://purl.stanford.edu/hf621yn0502.

[29] Ananth Saran Yalamarthy et al. “Significant Phonon Drag Enables High Power Factor in the AlGaN/ GaN Two-Dimensional Electron Gas”. In: *Nano Lett* 19 (2019), pp. 3770–3776. DOI: 10.1021/acs.nanolett.9b00901. URL: https://pubs.acs.org/doi/10.1021/acs.nanolett.9b00901..

[30] Pengfei Shao et al. “High density polarization-induced 2D hole gas enabled by elevating Al composition in GaN/AlGaN heterostructures”. In: *Applied Physics Letters* 122.14 (Apr. 2023). ISSN: 00036951. DOI: 10.1063/5.0139158/2882362. URL: /aip/apl/article/122/14/142102/2882362/High-density-polarization-induced-2D-hole-gas.

[31] N. A. Sidorenko and Z. M. Dashevsky. “Cryogenic Thermoelectric Cooler for Operating Temperatures below 90 K”. In: *Semiconductors* 53.6 (June 2019), pp. 752–755. ISSN: 10637826. DOI: 10.1134/S1063782619060216/FIGURES/4. URL: https://link-springer-com.tudelft.idm.oclc.org/article/10.1134/S1063782619060216.

[32] Alexander Sztein et al. “Calculated thermoelectric properties of InxGa1-xN, InxAl1-xN, and AlxGa1-xN”. In: *Journal of Applied Physics* 113.18 (May 2013), p. 183707. ISSN: 00218979. DOI: 10.1063/1.4804174/1014264. URL: /aip/jap/article/113/18/183707/1014264/Calculated-thermoelectric-properties-of-InxGa1-xN.

[33] Alexander Sztein et al. “Polarization field engineering of GaN/AlN/AlGaN superlattices for enhanced thermoelectric properties”. In: *Applied Physics Letters* 104.4 (Jan. 2014), p. 42106. ISSN: 00036951. DOI: 10.1063/1.4863420/379768. URL: /aip/apl/article/104/4/042106/379768/Polarization-field-engineering-of-GaN-AlN-AlGaN.

[34] Adam L. Woodcraft and Adam Gray. “A low temperature thermal conductivity database”. In: *AIP Conference Proceedings* 1185 (2009), pp. 681–684. ISSN: 0094243X. DOI: 10.1063/1.3292433. URL: https://www.researchgate.net/publication/259676995_A_low_temperature_thermal_conductivity_database.

[35] Ananth Saran Yalamarthy et al. “Tuning Electrical and Thermal Transport in AlGaN/GaN Heterostructures via Buffer Layer Engineering”. In: *Advanced Functional Materials* 28.22 (2018), p. 1705823. ISSN: 1616-301X. DOI: 10.1002/adfm.201705823. URL: https://dx.doi.org/10.1002/adfm.201705823.

[36] Ananth Saran Yalamarthy1 and 3 Debbie G Senesky2. “Strain- and temperature-induced effects in AlGaN/GaN high electron mobility transistors”. In: (2016). DOI: 10.1088/0268-1242/31. URL: https://dx.doi.org/10.1088/0268-1242/31.

[37] Jiabin Yan et al. “Review of Micro Thermoelectric Generator”. In: *Journal of Microelectromechanical Systems* 27.1 (Feb. 2018), pp. 1–18. ISSN: 10577157. DOI: 10.1109/JMEMS.2017.2782748.

[38] Qihao Zhang et al. “Micro-thermoelectric devices”. In: (2022). DOI: 10.1038/s41928-022-00776-0. URL: https://doi.org/10.1038/s41928-022-00776-0.

[39] Elbara Ziade et al. “Thickness dependent thermal conductivity of gallium nitride”. In: *Applied Physics Letters* 110.3 (Jan. 2017). ISSN: 00036951. DOI: 10.1063/1.4974321.

[40] J. Zou et al. “Thermal conductivity of GaN films: Effects of impurities and dislocations”. In: *Journal of Applied Physics* 92.5 (Sept. 2002), pp. 2534–2539. ISSN: 0021-8979. DOI: 10.1063/1.1497704. URL: /aip/jap/article/92/5/2534/471687/Thermal-conductivity-of-GaN-films-Effects-of.

[41] Nurkhaizan Zulkepli et al. “Review of Thermoelectric Generators at Low Operating Temperatures: Working Principles and Materials”. In: *Micromachines* 12.7 (July 2021). ISSN: 2072666X. DOI: 10.3390/MI12070734. URL: /pmc/articles/PMC8303398/%20/pmc/articles/PMC8303398/?report=abstract%20https://www.ncbi.nlm.nih.gov/pmc/articles/PMC8303398/.

A

Measurement error determination

To consider the measurement uncertainty during the measurement, the relative error must be determined by both the Seebeck coefficient and sheet resistance measurement. Using the relative error theory and stochastic addition of errors, the measurement uncertainty of the equipment used can be plotted as Error graphs.

Firstly, the Seebeck coefficient is calculated using Equation 5.2, in which the uncertainty of the multimeter and temperature sensors must be determined. The maximum error can be calculated using Equation A.1 where V_{re} represents the relative error of the measured Voltage and T_{re} the temperature relative error. These are calculated as described in Equation A.2, where ΔV represents the known uncertainty of the measurement equipment, and V is the measured quantity. This theory applies to V_{re} and T_{re}, where the relative error T_{re} is given in Equation A.3.

$$S_{error} = \pm S \cdot \sqrt{V_{re}^2 + T_{re}^2} \tag{A.1}$$

$$V_{re} = \frac{\Delta V}{V} \tag{A.2}$$

$$V_{re} = \frac{\Delta(\Delta T)}{\Delta T} \tag{A.3}$$

As the Seebeck coefficient measurement results change over different temperature differences, the relative error also changes. For example, the relative error for the temperature sensors, calculated using $T_{re} = \frac{\Delta(\Delta T)}{\Delta T}$ where $\Delta T = 2K$ decreases as a higher temperature difference is reached. Therefore, during the Seebeck coefficient measurements, a higher temperature difference over the die results in a lower relative error.

A similar approach is carried out to determine the sheet resistance measurement error, where Equation A.4 shows the total error margin calculation. Where V_{re} represents the same multimeter relative error, and I_re the relative error of the current source, which is calculated in the similar method as V_{re} and T_{re}.

$$Rsh_{error} = \pm Rsh \cdot \sqrt{V_{re}^2 + I_{re}^2} \tag{A.4}$$

During the Seebeck coefficient measurements, the following measurement uncertainties were taken into account:

- Temperature sensor uncertainty $\Delta(\Delta T) = \pm 2K$, from DT670 datasheet
- Keithley multimeter uncertainty $\Delta V =$, from Keithley 2002 datasheet offset current combined with expected resistance of the die

During the sheet resistance measurements, the following measurement uncertainties were taken into account:

- Keithley multimeter uncertainty $\Delta V =$, from Keithley 2002 datasheet offset current combined with expected resistance of the die

- Yokogawa SMU current source uncertainty $\Delta I = 0.1\mu A$, from Yokogawa GS210 datasheet

The PF error is calculated in a similar method, in which the relative error of the Seebeck coefficient measurement and sheet resistance measurement are used to determine the total error as seen in Equation A.5.

$$PF_{error} = \pm PF \cdot \sqrt{(2 \cdot \frac{\Delta S}{S})^2 + (\frac{\Delta Rs}{Rs})^2} \tag{A.5}$$

B

Complete flow-chart of fabrication process

Flowchart

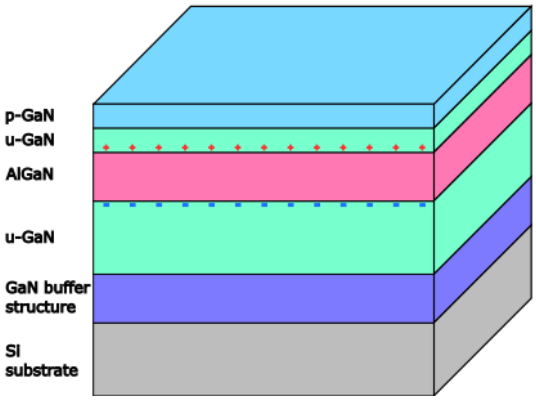
Lex Pardon

Last updated: 27-09-24

Number of Wafers: 1 (4-inch)

General stackup, from top to bottom:

1. P-type GaN, 30 nm, doped with Mg 3E19 cm-2
2. Undoped GaN, 20 nm
3. AlGaN, thickness 50 nm and Al content 20%
4. Undoped GaN, 1.6 um
5. GaN/AlGaN buffer structure
6. Si Substrate



1. **Inspect wafer**

   Tool: Optical microscope
   Goal: Inspect status of surface for imperfections/cracks
   Take pictures and document of points of interest

2. **Apply Photo-resist**

Tool:	Manual spin-coater, 4-inch wafer chuck
Recipe/PR:	S1805
Spin speed:	1000 rpm
Goal:	Protect wafer from dust during dicing process

3. **Pre-bake photo-resist**

Tool:	Hotplate
Temperature:	95 C
Time:	1 minute

4. **Dice wafer**

Tool:	Disco dicer
Size:	25 x 25 mm dies

   Appendix D shows dicing map
   Note: Dices placed in similar pattern in die-box to keep documented points of interest easy to find

5. **Remove Photo-resist**

   DMSO, 30 min @ 80 C
   Acetone, 1 minute
   IPA, 1 minute, 2 times
   DI, 1 minute, 2 times
   Blow Dry with Nitrogen gun

   Repeat if nescasary

6. **Inspect Dies individually**

   Tool: Optical microscope
   Goal: - Find and filter out badly diced die's for rough edges
   - Verify complete removal of photo-resist
   Document unusable dies
   Take pictures of points of interest on individual dies

7. **NH4OH dip**

   NH4OH:H20 – 1:20 diluted, 10 seconds
   Dip/Rinse in H20 After (5 min.)
   Blow-dry with N2 gun

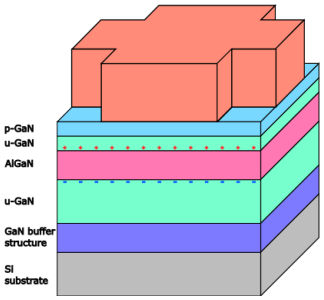
8. **Dehydrate**

   Tool: Hotplate
   Temperature: 90 C
   Time: 1 min

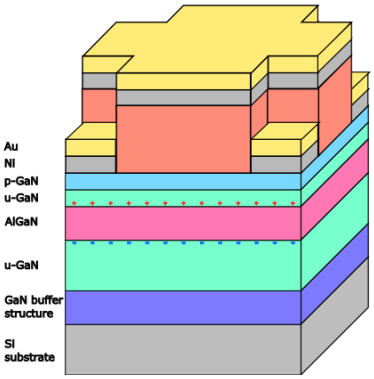
9. **Apply tape / sharpie**

   Apply kapton tape (precut)

   Image as example illustration only



10. Evaporate Ni/Au

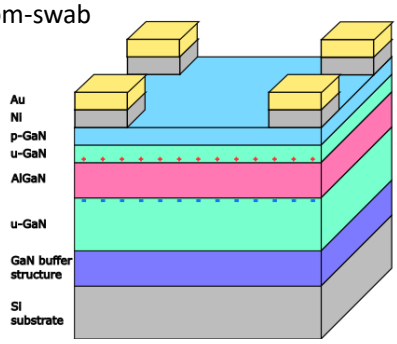


Tool: Leybold L560
Metals: Ni/Au
Thickness: 20/100 nm
Min. Vacuum: 1E-6 mbar
During loading:

- Ni and Au crucables must be loaded into corresponding pockets
- Sample mounted with spring-clamps on the tape to prevent shadowig contacts

11.Remove tape and residue

Remove tape using:
Acetone, scrub residue with cleanroom-swab
IPA, 5 minutes
DI, 5 minutes
Blow dry with N2 gun
Repeat if nessecary



12.Inspect Die

Tool: Optical microscope
Goal: - Verify complete removal of tape and residue
- Determine quality of metal deposition
- Verify that metals are on correct location on die

Document and take pictures of points of interest

13. Thermal Annael metal contacts

Tool:	Oven (Located in EKL)
Temperature:	550 C
Environment:	Ambient air, no extra added gasses
Time:	10 min.
Note:	Requires pre-heating of oven before loading sample
	Samples loaded on carrier Si wafer

14. Inpsect die

Tool: Optical microscope
Goal: Inspect status of surface for imperfections
Take pictures and document of points of interest

15. Apply second shadowmask using kapton tape

Apply kapton tape (precut)
Allign with previously deposited metals to minimize mismatch

16. Evaporate Ti/Au

Tool:	Leybold L560
Metals:	Ti/Au
Thickness:	10/200 nm
Min. Vacuum:	1E-6 mbar

During loading:

- Ti and Au crucables must be loaded into corresponding pockets
- Sample mounted with spring-clamps on the tape to prevent shadowig contacts

17. Remove tape and residue

Remove tape using:
Acetone, cotton-swab
IPA, 5 minutes
DI, 5 minutes
Blow dry with N2 gun
Repeat if nessecary

18.Inspect Die

Tool:	Optical microscope
Goal:	- Verify complete removal of tape and residue - Determine quality of metal deposition - Verify that metals are on correct location on die

Document and take pictures of points of interest

19. Apply Photo-resist as protective layer for redicing

Tool:	Manual spin-coater, wetbench area
Recipe/PR:	S1805
Spin speed:	1000 rpm
Goal:	Protect wafer from dust during dicing process

20.Pre-bake photo-resist

Tool:	Hotplate
Temperature:	95 C
Time:	1 minute

21.Dice wafer

Tool:	Disco dicer
Size:	25 x 5 mm strips from previous 25x25 mm dies

22.Remove Photo-resist

DMSO, 30 min @ 80 C
Acetone, 1 minute
IPA, 1 minute, 2 times
DI, 1 minute, 2 times
Blow Dry with Nitrogen gun

Repeat if nescasary

23. **Inspect strips**

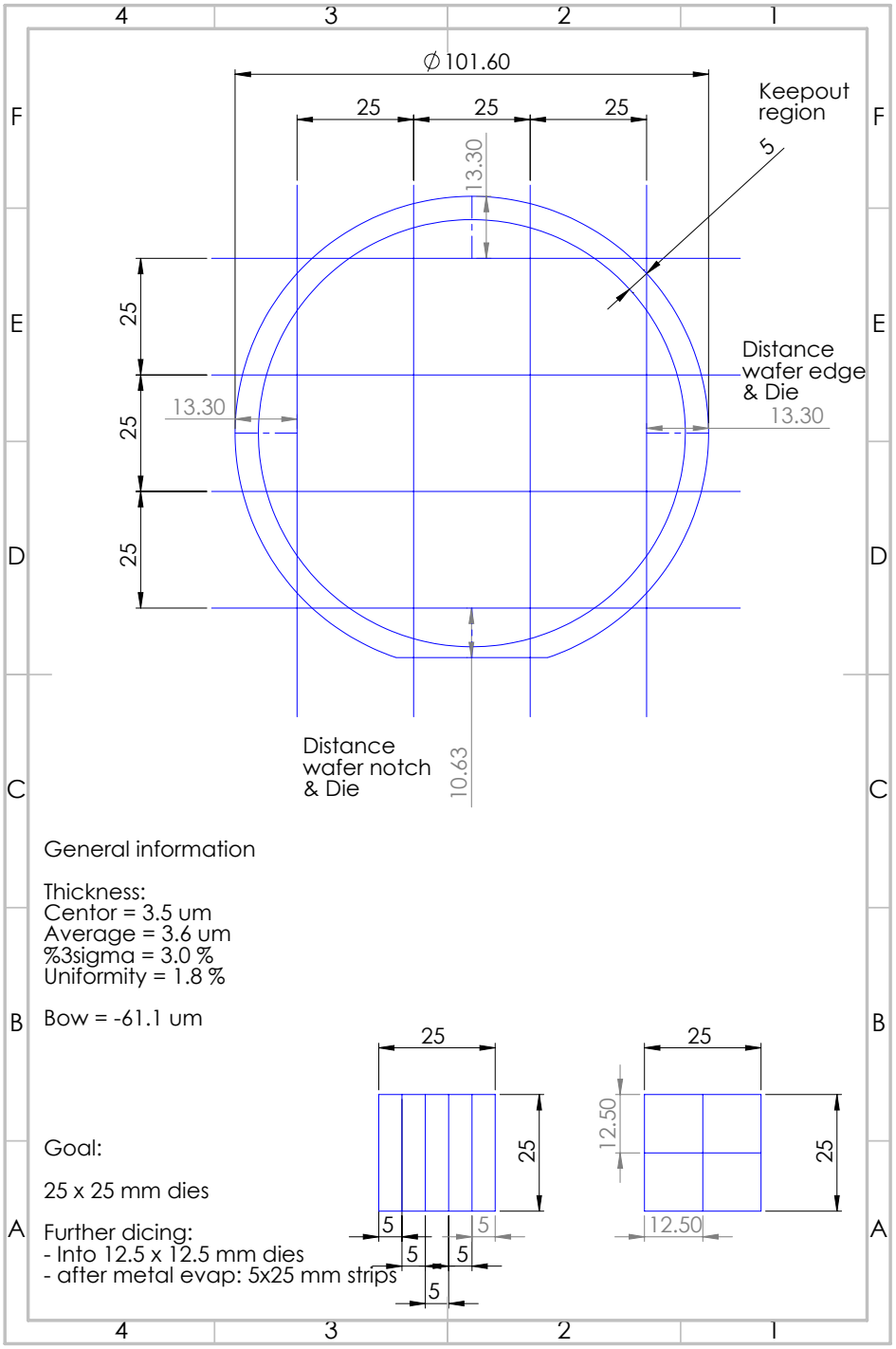
Tool:	Optical microscope
Goal:	- Verify complete removal of Photo-resist - Determine quality of metal deposition - Verify that metals are alligned to other metals

Document and take pictures of points of interest

The 25x5 mm strips are now ready to be glued and bonded onto the PCB

C

Dicing map


∅101.60
25
25
25
Keepout region
5
13.30
25
25
25
13.30
Distance wafer edge & Die
13.30
Distance wafer notch & Die
10.63
General information
Thickness:
Centor = 3.5 um
Average = 3.6 um
%3sigma = 3.0 %
Uniformity = 1.8 %
Bow = -61.1 um
Goal:
25 x 25 mm dies
Further dicing:
- Into 12.5 x 12.5 mm dies
- after metal evap: 5x25 mm strips
25
25
5
5
5
5
5
25
25
12.50
12.50
25

D

Cryo-cooler user guide

To be able to use the cryocooler, it is important that the user reads this short guide on how to use the cryocooler setup. This how to guide is split into two different sections:

- Overview of equipment required to operate the cryocooler
- A step-by-step guide on how to use the cryocooler in the same order as one would use the setup.

D.1. Equipment

The cryo-cooler setup consists of the following equipment:

- A vacuum chamber with a Stirling cooler mounted to it and a vacuum valve to decouple the hose
- An electronics box to control the Stirling cooler, powered by a 110-240 V transformer because the controller is American-made
- A vacuum pump cart consisting of a diaphragm and turbomolecular pump, including a pump controller
- A vacuum hose to connect the vacuum pump to the chamber
- A vacuum gauge, to measure the vacuum level, currently read out using an Arduino

D.2. Using Procedure

The usage of the cooler is split into different steps:

1. Opening the vacuum chamber, mounting the sample
2. Pumping down to deep vacuum
3. Cooling down, and controlling the cryo-cooler
4. Warming up and opening again
5. Long-time storing the cooler

D.2.1. Opening the vacuum chamber, mounting and closing the vacuum

In case the chamber has not been used for a while, it is most likely still under vacuum, with the valve to the vacuum hose closed. To be able to open the front of the vacuum air must slowly be let into the chamber by slowly opening the valve, when the vacuum pump is turned off. If the valve was open and the vacuum pump turned on, the vacuumpump can be turned off. This will let in air slowly automatically controlled by the vacuumpump controller.

Warning: It is important that the cryo-cooler is turned off and has warmed up to room temperature to avoid condensation inside the chamber.

The Front window of the vacuum chamber can now be unscrewed with a 3.5 mm hex screw to mount your sample.

Several cables are already connected to the connector to the outside, it is recommended to check for continuity and validating which cable is connected to which part of your sample before closing the chamber again.

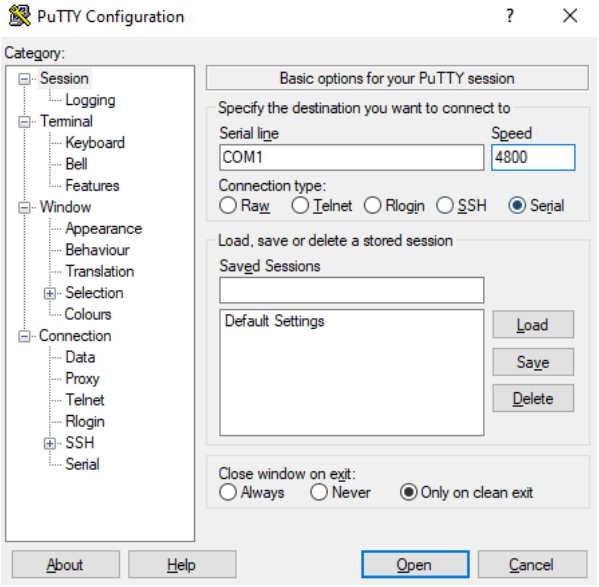


Figure D.1: Putty settings, COM-port can change

D.2.2. Closing the chamber and pumping down to vacuum

When your sample is mounted, the front can be closed again. When everything is closed, make sure the black vacuum valve on the vacuum chamber is opened so that the vacuum-pump is able to evacuate the air out of the chamber.

Warning: It is important to note that once the vacuum-pump is turned on, it is not able to move the setup anymore because the turbo-pump is spinning at extreme speeds and can therefore easily break when moved around.

Warning: Once the turbopump is running on full speed, a sudden exposure to non-vacuum can break the pump. Make sure the vacuum valve to the chamber was already open. If not, but the vacuum pump is already running, turn the vacuum off, wait several minutes, open the valve and then start running the vacuum pump again

The vacuumpump can be turned on once everything is closed and verified, it will take several hours to reach a vacuum of 5E-5 mbar. It is recommended to do this overnight

To read the vacuum-gauge, the powersupply connected to the gauge must be turned on and the arduino must be connected to the PC. The screen attached to the Arduino should turn on, showing the pressure after a few seconds. It is possible to connect with the Arduino through a serial com-port at a baudrate of 9600, Sending a 'P' command, will return the pressure (useful for logging)

D.2.3. Cooling down, controlling the cryo-cooler

Warning: It is important a good vacuum has been reached to increase efficiency and prevent moisture buildup on samples

A minimal vacuum of 5E-5 is required before turning the cooler on.

Connect the USB from the controller box to a computer, and use PUTTY or other serial COM-port communication software to connect to the cooler with a baud-rate of 4800. A terminal should open, in which commands can be sent. A list of commands can be found below, X represents a chosen input.

- SSTOP=X, X=1 is softstopping the cooler, X=0 is starting the cooler
- TC, returns the cooler temperature
- SET TTARGET=XXX.XX, sets target to XXX.XX Kelvin (example: SET TTARGET=050.00)
- P, returns the power the cooler is currently using

D.2.4. Warming up and opening again

When a measurement is done or a warmup cycle must be started, the SSTOP=1 command must be sent to the cooler. It will then take at least 24 hours to warm up. Ideally, at least 2 days of warmup to

get to room temperature.

It is then possible to open te cooler again **Important:** make sure that the inside temperature is at room temp again.

D.2.5. Long-time storage

When the vacuum chamber is planned not to be used for a while, ideally the vacuum pump is turned off with the chamber on vacuum. In order to do so, a high vacuum must first be applied by turning the vacuum pump on for 1 day minimum (5E-5 mbar). The vacuum-chamber valve can then be closed to de-couple the chamber from the vacuum pump. The vacuum pump can then be turned off.

D.3. Other notes

It must be noted that all COM-ports can also be controlled using a Python script using the pyserial package. It can then be possible to control and read out the cooler, as well as read out the vacuum level using the arduino

Inside the chamber, 3 DT670 Diode temperature sensors are placed. And are connected through the connectors. In order to read those out, an SMU with 4-wire measurement capabilities is required. By applying a current of 10 micro-Amps onto the leads and measuring the voltage on the same leads, the temperature can be looked up in a lookup table. The lookup table can be found on the Lakeshores website.